Generating a Mouse Model of Symptomatic and Asymptomatic Intracerebral Hemorrhage by Applying High-Pressure Focused Ultrasound

Crystal Marie Destiny Collier

Submitted in partial fulfillment of the
requirements for the degree of
Doctor of Philosophy
under the Executive Committee
of the Graduate School of Arts and Sciences

COLUMBIA UNIVERSITY

2021

Abstract

Generating a Mouse Model of Symptomatic and Asymptomatic Intracerebral Hemorrhage by Applying High Pressure Focused Ultrasound

Crystal Marie Destiny Collier

Intracerebral hemorrhage defines a category of neurological disease that spans the full range of possible clinical outcomes. At one end of the spectrum is hemorrhagic stroke, an oftendebilitating neurologic condition with substantial morbidity and mortality while cerebral microhemorrhage at the other end of the spectrum can go completely unnoticed as they are often asymptomatic. Despite the distinct clinical outcomes both conditions share a common risk factor, uncontrolled hypertension. Here we set out to generate a novel mouse model of intracerebral hemorrhage with pressure as the mode of hemorrhage induction. To conduct our studies, we utilize high pressure focused ultrasound in combination with injected microbubbles to cause hemorrhage. We applied this technique at two different pressures resulting in striatal hemorrhage induction with distinct phenotypic outcomes. Following induction at the higher-pressure, mice show evidence of lateral motor deficit and other signs of impairment. Mice with hemorrhage induced at the lower pressure show no behavioral signs of neurological deficit. We employ immunofluorescence and western blotting to understand the cellular responses to intracerebral hemorrhage in these mice. We find evidence of inflammation and cell death following high-pressure induction of intracerebral hemorrhage. Lower pressure induction of intracerebral hemorrhage lacks signs of cell death but shows apparent inflammation. We have created a novel

pressure-dependent mouse model of symptomatic and asymptomatic intracerebral hemorrhage by applying high intensity focused ultrasound in combination with circulating microbubbles.

Table of Contents

List of Figures and Tables

List of Abbreviations and Acronyms

APAF1: apoptotic protease activating factor 1

ATACH: Antihypertensive Treatment of Acute Cerebral Hemorrhage Trial

ATACH II: Antihypertensive Treatment of Acute Cerebral Hemorrhage II Trial

BME: beta mercaptoethanol

cl casp 3: Cleaved caspase 3

CT: Computed Tomography

DAM: disease associated microglia

FUS-ICH: Focused Ultrasound-Induced Intracerebral hemorrhage

FUS-ICH 1.5: Focused Ultrasound-Induced Intracerebral hemorrhage at 1.5 MPa

FUS-ICH 2.5: Focused Ultrasound-Induced Intracerebral hemorrhage at 2.5 MPa

FUSO: Focused Ultrasound Only

GD: gadolinium

GFAP: Glial Fibrillary Acidic Protein

H&E: Hematoxylin and Eosin

IAPs: inhibitors of apoptosis

i-DEF: The Deferoxamine mesylate in patients with intracerebral hemorrhage Trial

LAMP: lysosomal associated membrane protein

MRI: Magnet Resonance Imaging

PBS: Phosphate Buffer Solution

PL: Pulse length

pMLKL: phosphorylated Mixed Linkage Kinase domain Like pseudokinase

PRF: Pulse repetition Frequency

ROS: reactive oxygen species

STICH: The Surgical Treatment of Intracerebral Hemorrhage Trial

T1W MRI: T1 Weighted MRI

T2W MRI: T2 weighted Magnet Resonance Imaging

TBS: Tris-Buffered Saline

TPA: Tissue plasminogen antigen

TUNEL: Terminal dUTP Nick End Labeling

Acknowledgments

Many are deserving of acknowledgement for their support during the execution of this work. I would like to acknowledge my mentor Dr. Carol Troy, the members of the Troy lab, Dr. Yuji Mishina, Dr. Haoxing Xu, Dr. Hilda Hutcherson, the MSTP Coordinators, my Thesis Committee Members Dr. Dritan Agalliu, Dr. James Goldman, Dr. E. Sander Connolly, Dr. Elisa Konofagou, the Konofagou lab, and my family Timothy Collier Sr., Charline Collier, Timothy Collier Jr., Gabrielle Collier, Maya Collier, Layla Collier, and Michael Ashley.

Dedication

To **Maya Simone Destiny Collier** and **Layla Jean Collier**

Always know that there are no limits

to what you can achieve.

Chapter 1: Introduction

1.1 Neurologic disease: stroke

Stroke, the broad term referring to compromised blood flow within a region of the brain resulting in acute focal neurologic impairment, is also referred to as a cerebrovascular accident[1]. Originally identified symptomatically, imaging such as Computed Tomography (CT) and Magnetic Resonance Imaging (MRI) have allowed further identification of what is broadly considered stroke into categories based on mechanism of brain injury[1-4]. These categories include ischemic and hemorrhagic stroke. Hemorrhagic stroke is further subcategorized into subarachnoid hemorrhage and intracerebral hemorrhage based on the site of origin of the hemorrhage[2].

The predominant subtype of stroke is ischemic, accounting for approximately 80% of stroke incidence[1]. Ischemic stroke is a condition in which an artery within the brain is occluded either by thrombus or embolism resulting in a lack of perfusion to the brain region supplied by the affected artery[1]. If the blockage of the blood vessel is transient, the result may be a transient ischemic attack defined as a focal neurologic deficit lasting up to 24 hours[1]. More long-lasting blockages can cause ischemic stroke. The presentation depends on the blood vessel that is blocked, and which brain region is impaired. Outcomes can include hemiparesis and hemiparalysis, hemineglect, speech difficulty, blindness, and loss of coordination for blockages affecting the cerebral cortex, and cerebellum respectively[5].

Risk factors for stroke include advanced age, hypertension, diabetes, and smoking[1, 6-8]. Ischemic stroke is a neurologic emergency requiring rapid identification and treatment[9]. Prolonged duration of cerebral hypoperfusion is associated with increased cellular death and neurologic dysfunction[1]. Potential treatment modalities include pharmacologic and mechanical

interventions. Tissue plasminogen antigen (TPA) has been long appreciated for the ability to reverse the effects of ischemic stroke if administered within the treatment window [9]. Endovascular interventions to remove clots involved in ischemic stroke have gained popularity[10].

Hemorrhagic transformation represents a critical complication of ischemic stroke previously seen in up to 43% of ischemic stroke patients[11, 12]. Hemorrhagic transformation is associated with worsened outcomes therefore a fine balance must be achieved between the prevention of excessive coagulation and the prevention of hemorrhage[9, 13, 14]. This complication limits options for ischemic stroke treatment and prevention of recurrence as interventions to eliminate clots and reduce coagulation have substantial potential to promote hemorrhage[9, 11, 15-18]. Due to the relationship between treatment of ischemic stroke and induction of hemorrhage, an improved understanding of intracerebral hemorrhage poses potential beneficial for treatment and secondary prevention of ischemic stroke.

1.1.1 Intracerebral hemorrhage

Intracerebral hemorrhage includes hemorrhagic stroke, subarachnoid hemorrhage and cerebral microbleed[2]. Although less prevalent than ischemic stroke, hemorrhagic stroke accounts for a large portion of stroke mortality and morbidity and has been determined to be a major contribution to neurologic disease burden globally[19, 20]. For these reasons the understanding of hemorrhagic stroke and the development of new therapeutic options are of high interest.

Figure 1.1: Global Burden of Neurologic Disease

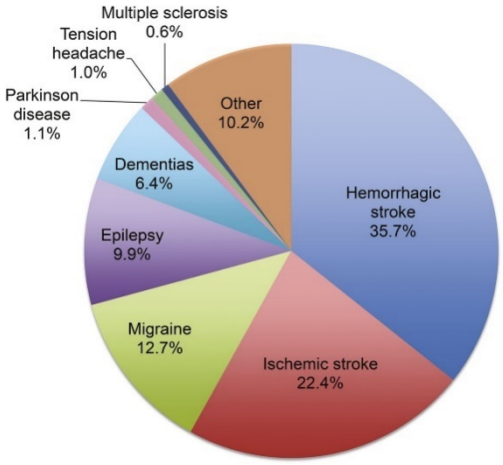

Contribution of specific causes to the combined burden of neurologic disorders and cerebrovascular disease (percent of total disability-adjusted life-years)
Source: GBD 2010 Results by Cause 1990–2010.

Global burden of neurologic disease by disability adjusted life-years shows 35.7% of the burden of neurologic is caused by hemorrhagic stroke. Adapted from [19]

Although hemorrhagic stroke has been a subject of intense study for decades, there exist few treatment options for patients suffering from this stroke subtype[21-23]. The pathophysiology of hemorrhagic stroke remains incompletely understood however clues from risk factors have informed current beliefs about the origin of spontaneous intracerebral hemorrhages[2, 24].

The pathophysiology of primary spontaneous hemorrhagic stroke is believed to begin with prolonged elevated intravascular pressure within the intracerebral arteries[25]. Under the constant pressure, the walls of the blood vessels weaken and subsequently rupture sending blood products into the brain parenchyma[25]. This leads to the formation of a hematoma that may compress brain structures resulting in a mass effect, known as the primary injury. The hematoma and surrounding edema also may compress the surrounding vasculature causing a region of ischemia[24]. The breach of the blood brain barrier triggers inflammation and cell death within

the region affected by the hemorrhage contributing to pathology known as the secondary injury[26].

Figure 1.2: Pathophysiology of intracerebral hemorrhage

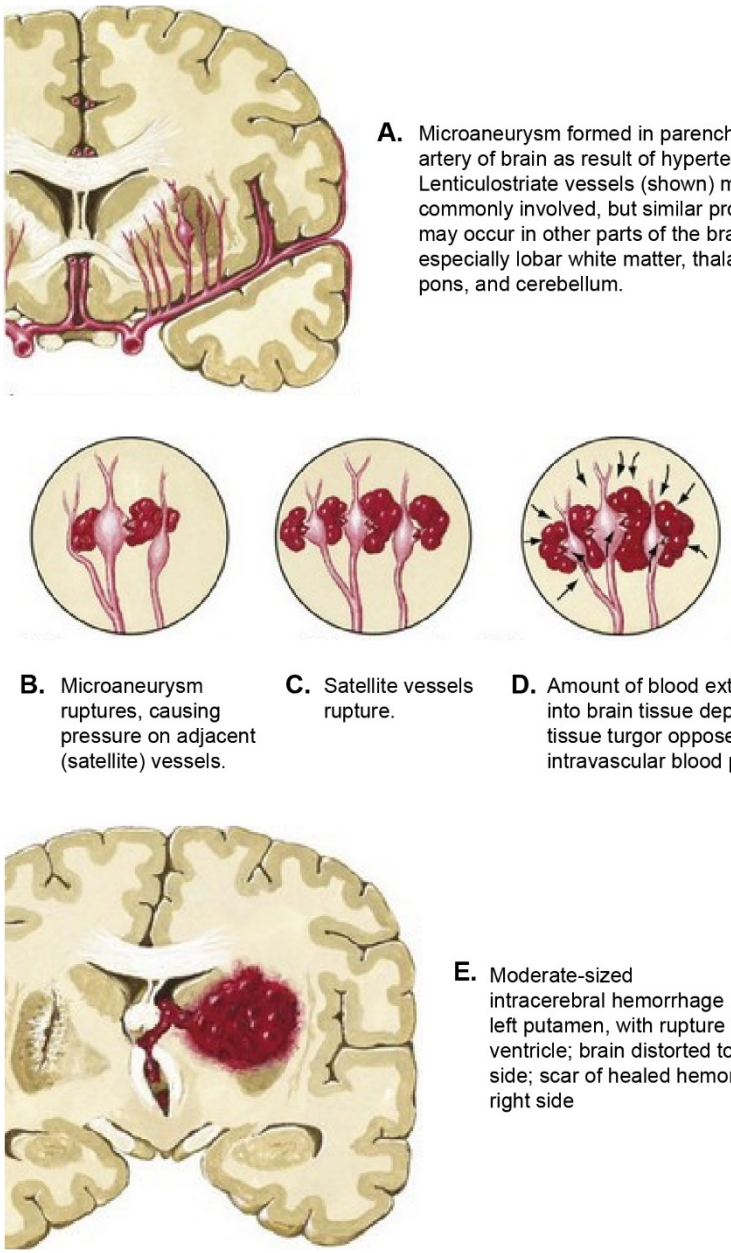

Schematic representation of the pathophysiology of intracerebral hemorrhage. Adapted from [25]

Hemorrhagic stroke is classified as primary or secondary depending on an origin that is spontaneous or due to a pre-existing condition respectively[1, 24]. The majority of hemorrhagic

stroke cases are of the primary subtype occurring within the deep structures of the brain such as the striatum[27]. Predisposing factors for primary hemorrhagic stroke include age, hypertension, and geographic location[8, 20]. The rising use of anticoagulation is also believed to contribute to the prevalence of intracerebral hemorrhage[14].

Sex differences have been noted in intracerebral hemorrhage incidence with females showing a lower incidence than males within most stratified age groups[28]. Estrogen has been noted to reduce edema resulting from iron exposure and poses a potential mechanism for neuroprotection in females[29].

Outcomes following intracerebral hemorrhage are predicted by factors including the initial hemorrhage volume, hematoma location, hematoma expansion, the Glasgow Coma Score, the presence of intraventricular hemorrhage and age of the patient[1, 2, 12, 22]. Clinical evaluation of intracerebral hemorrhage includes imaging with Computed Tomography (CT) or Magnet Resonance Imaging (MRI)[3, 22]. On contrast enhanced CT there may be a focal region of hyperdensity corresponding to contrast extravasation. This finding, referred to as the spot sign, is associated with hematoma expansion[12]. Hematoma expansion, defined as an increase of hematoma volume by 33% from initial imaging, is associated with increased mortality and morbidity following hemorrhagic stroke[30]. On MRI, the appearance of intracerebral hemorrhage varies over time due to changes in the magnetic properties of the hematoma[31].

1.1.2 Hemorrhagic stroke therapies and clinical studies

Hemorrhagic stroke is a clinical emergency requiring immediate evaluation and intervention[24]. The mass effect following hemorrhagic stroke has the potential to cause herniation of brain structures resulting in severe neurologic dysfunction and death[22, 32, 33]. Clinical management of intracerebral hemorrhage involves initial diagnosis via clinical suspicion

confirmed by imaging with either MRI or CT[2, 21, 22]. Current therapies for hemorrhagic stroke are largely supportive including blood pressure correction and monitoring of intracranial pressure[21-23, 34].

The approach to treatment of intracerebral hemorrhage is informed by numerous clinical studies on the subject[33, 35, 36]. Over 280 clinical trials have been reported involving intracerebral hemorrhage with the goal of developing a better understanding of disease progression and testing potential therapeutic interventions. Key trials that influence modern understanding and treatment of intracerebral hemorrhage include the Antihypertensive Treatment of Acute Cerebral Hemorrhage (ATACH) trial and the Surgical Treatment of Intracerebral Hemorrhage (STICH) trial[35, 37].

Since the initial finding of the ATACH trial that early blood pressure control is beneficial to patients, there have been various additional trials and subgroup analyses seeking to address the optimal timing, populations, and goals of blood pressure control in ICH patients[35, 36, 38-40]. The ATACH II trial compared an intensive blood pressure goal (systolic blood pressure of 110-139) to standard control (systolic blood pressure of 140-179) finding no difference in mortality or disability between the two groups[36]. Subgroup analysis of the ATACH-2 trial demonstrates a reduction of hematoma expansion and overall hematoma size following spontaneous basal ganglia ICH however the functional outcomes were not altered[27]. There is interest in utilizing the spot sign to stratify patients likely to benefit from treatments such as intensive blood pressure control[41].

Surgical removal of the hematoma was shown to have little benefit when applied broadly to ICH populations in the STICH trial[37]. Surgical treatment in intracerebral hemorrhage remains an active area of study with the goal of identifying patients likely to benefit[42-45].

Various neuroprotective agents have been targeted following promising results in preclinical studies including minocycline and deferoxamine[46-48]. However further studies are needed to determine potential efficacy in humans. Deferoxamine, an iron chelator has been shown to be beneficial in animal studies of intracerebral hemorrhage[49]. Clinical trials however have not seen the same success thus far. The Deferoxamine mesylate in patients with intracerebral hemorrhage (i-DEF) trial found safety in administration of deferoxamine in ICH patients but did not find sufficient efficacy to warrant a phase III trial[47]. The disconnect between the development of promising treatment options in preclinical research often conducted with rodent studies and the lack of efficacy in human trials details a need to better understand the key contributors of the disease to pathology as well as to understand how the models compare to human disease. There exists the need for additional animal models of intracerebral hemorrhage to facilitate understanding of critical elements of intracerebral hemorrhage pathophysiology

1.1.3: Cerebral microbleed

A cerebral microbleed is defined as one or more circular or elliptical areas of hemorrhage of 2-10mm in diameter on MRI imaging[50]. The increased use of cerebral imaging in addition to the application of more sensitive MRI sequences to imaging protocols have led to an increased appreciation for the prevalence of cerebral microhemorrhage[50]. Cerebral microbleeds are associated with vascular disease including hypertension and cerebral amyloid angiography[3, 50, 51]. They are also considered to be a predisposing factor for the development of intracerebral hemorrhage, ischemic stroke, and dementia. Inflammation has been found in cerebral microhemorrhage[52]. Although cerebral microhemorrhage is often asymptomatic, the prevalence of cerebral microbleeds in the setting of neurologic disease demonstrates the importance of understanding the associated pathology.

Figure 1.3: Cerebral microhemorrhages

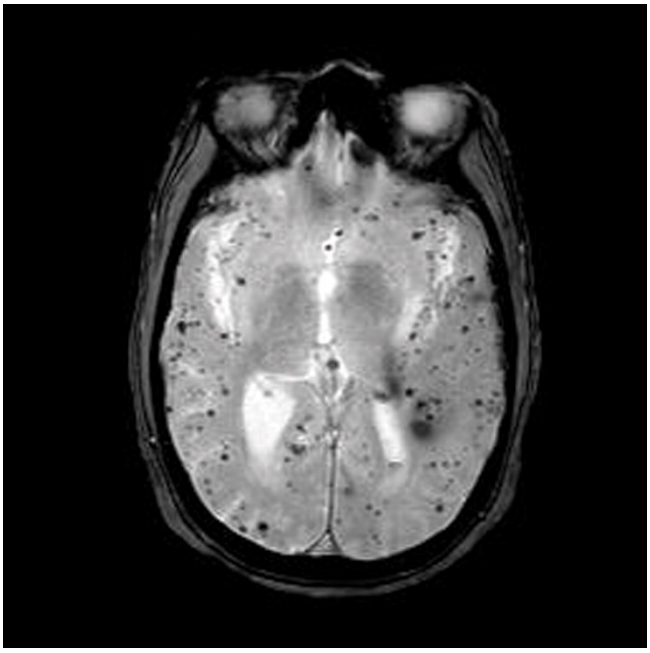

Axial MRI with numerous cerebral microhemorrhages**.**
Adapted from [53]

1.1.4 Mouse models of intracerebral hemorrhage

Animal models have been critical to our understanding of the pathophysiology of various diseases[54]. Categories of animal models of focal neurologic disease include inducible and spontaneous. In inducible models, pathology is directly caused by an intervention. Spontaneous models of disease often rely on replicating risk factors of the disease of interest predisposing mice to develop pathology.

Multiple rodent models of intracerebral hemorrhage have been created to probe the cellular and molecular pathways involved in intracerebral hemorrhage pathology[55]. The striatal balloon inflation technique initially described by Sinar et. al. involves the injection of a syringe surrounded by a balloon with subsequent inflation[56]. This model recreates the primary

effect of the pressure of the hematoma on the parenchymal structures resulting in cerebral blood vessel compression and ischemia however there is no blood toxicity or secondary injury of intracerebral hemorrhage[56]. This model is used less frequently as other models of hemorrhagic stroke have become increasingly favored.

Autologous blood injection was described by Ropper et al.[57]. This model is generated by obtaining blood and injecting it into the target region. The autologous blood injection model causes a mass effect and reproduces the effects of blood toxicity on the brain. The autologous blood injection model does not involve vascular damage[55, 57].

The collagenase injection model of hemorrhagic stroke described by Rosenberg et. al. is achieved by injecting bacterial collagenase into the target region[58]. The collagenase degrades the extracellular matrix leading to blood vessel rupture. This model induces the mass effect, toxic effects of blood and vascular rupture but does not involve increased intravascular pressure[55].

Spontaneous models of intracerebral hemorrhage exist that generate long standing hypertension in the mice and result in spontaneous intracerebral hemorrhage. Renal artery ligation in addition to a high salt diet are techniques employed to induce chronic hypertension in mice[55]. This technique is likely to closely replicate the pathophysiology of human intracerebral hemorrhage as the predisposing factor of prolonged elevated blood pressure is involved in both. The spontaneous nature of the development of intracerebral hemorrhage poses challenges for studying the development of pathology within these models. As the hemorrhage occurs spontaneously, it is difficult to know the time of hemorrhage onset.

There are both spontaneous and inducible models of cerebral microbleed[59]. Non-spontaneous induction of cerebral microhemorrhage involves laser-induced vessel ablation under the guidance of two photon imaging for vessel localization[60]. This model induces a single

microhemorrhage targeted to a vessel of interest[60]. The laser-induced cerebral microbleed model requires creation of a cranial window for two photon imaging of the target vessel. Due to the requirement of two photon imaging for identifying a target vessel, this technique is only applicable to cortical regions[59]. Spontaneous cerebral microbleeds are created via genetic overexpression of APP creating a model of CAA. Hypertensive mice are also used as a model of spontaneous intracerebral hemorrhage[59].

Although various mouse models of intracerebral hemorrhage exist, there remains a need for the development of additional models to further facilitate intracerebral hemorrhage research. The American Heart Association highlights areas of particular interest for novel models of intracerebral hemorrhage including inducible models, hemorrhage enlargement and resolution, with the ability to target different regions of the brain[61].

1.2 Neuroinflammation: Microglia and Astrocytes

Microglia are the resident immune cells of the central nervous system. Derived from cells in the myeloid lineage, microglia represent a unique cell type within the brain[62]. During homeostasis microglia exhibit a ramified morphology with a small cell body and numerous long processes with many branches[63]. This morphology facilitates constant surveillance of the surrounding environment[64].

Activation of microglia has been an active area of investigation. Morphological changes have been observed in microglia confronting a neurological insult[63]. Microglia in pathologic states have been found to have a more amoeboid morphology with fewer branches[63]. Additional assays of microglia have provided more detailed understanding of microglial reactions to neurologic pathology. CD68 is a lysosomal associated protein found in microglia thought to be associated with phagocytic activity within the microglia[65]. CD68 is found to

increase in microglia responding to disease states[65, 66]. RNA sequencing has allowed for further characterization of microglia in multiple states including the recognition of disease associated microglia (DAM)[67-71].

Figure 1.4 Schematic of microglial activation states

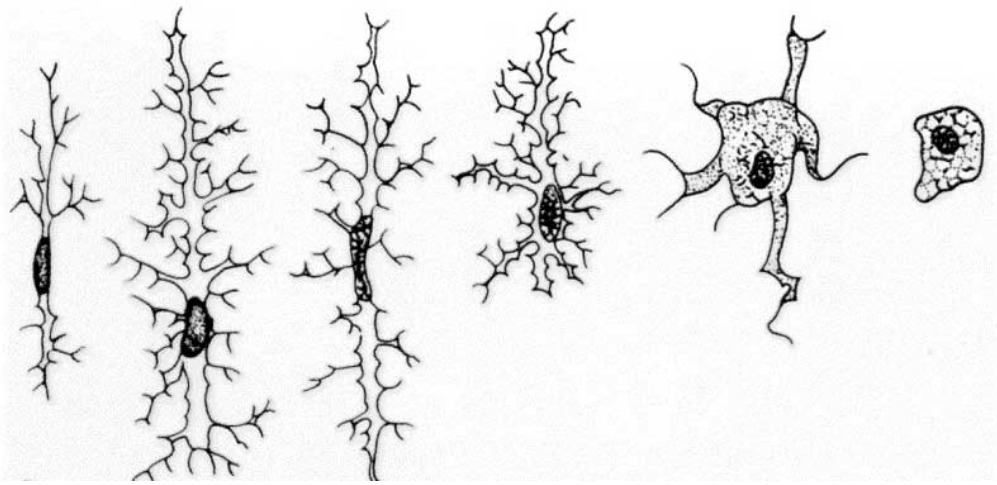

Representation of progressively activated Microglial states. Adapted from [72]

Early descriptions of the activation state of microglia described two distinct forms: M1 and M2 that promote increased inflammation or repair respectively[73, 74]. The accuracy of this microglial polarization paradigm has come into question. RNA sequencing and other methods of study have provided a more detailed understanding of the various microglial populations in existence replacing the M1 vs M2 classification scheme[68-70, 75].

Cultured microglia have been utilized to gain an understanding of the functions of this cell type in a more controlled environment. In culture microglia have been shown to require caspase 8 activity for activation[76]. Downstream caspases including caspase 7 and caspase 3 are

also required[76]. The response of microglia to hemorrhage has also been addressed. Animal models have demonstrated microglial response to intracerebral hemorrhage[77].

Microglia rely on constant colony stimulating factor CSF1 and CSF1R interaction for survival[78, 79]. Therefore, inhibition of CSF1R with compounds such as plx3397 create near complete depletion following treatment[80, 81]. Models of intracerebral hemorrhage in which microglia have been depleted prior to induction of intracerebral hemorrhage demonstrate a reduction in the size of the hematoma[80]. This finding suggests that the role of microglia in the pathophysiology of intracerebral hemorrhage goes beyond hematoma clearance and is capable of contributing to the development of larger rather than smaller hematomas. The suggestion of an adverse impact of microglia has led to an interest in reducing the effect of microglia on intracerebral hemorrhage with the goal of reducing the size of the hematoma and improving outcomes[82]. Animal models have demonstrated benefit in potential therapeutic options that show reduced microglial activation including minocycline and pioglitazone[83, 84].

Astrocytes are an abundant cell type within the brain now recognized for having various essential roles within the central nervous system[85]. Astrocyte end feet form a critical component of the blood-brain barrier[86]. Astrocytes have been found to be involved in various disease processes including stroke, multiple sclerosis, and Alzheimer's Disease[82, 85, 87, 88]. Similar to microglia, there have been studies assessing the differences between astrocytes in the healthy brain and astrocytes in disease states[85]. Astrocytes are noted to undergo morphological changes in the setting of pathology appreciable by labeling with the astrocyte marker GFAP[89]. In physiologic conditions, astrocytes show a highly branched, stellate, morphology[90]. Disease states have shown shift toward hypertrophic astrocytes and upregulation of GFAP[90].

1.3 Cell death pathways

The regulation of cell death is a critical function to maintain the integrity of an organism[91]. While excessive cell death is a contributing factor to diseases such as neurodegeneration, inadequate cell death can facilitate uncontrolled cellular proliferation, a feature of cancer pathogenesis[91, 92]. Therefore the appropriate balance must be achieved in order to ensure the health of the organism.

Long studied forms of cell death include necrosis and apoptosis[91, 93]. Lately cell death pathways with differing components and hallmarks have been identified including pyroptosis, necroptosis, and ferroptosis[92, 94-99].

Apoptosis

Apoptosis is a highly regulated form of cell death. Cell death via apoptosis results in little impact on the surrounding environment of the cell[91]. Cells enter apoptosis through one of two major pathways termed the intrinsic and the extrinsic pathway[91]. Cytotoxic signals trigger a cascade of protein changes within the mitochondria. Critical components include cytochrome C, apoptotic protease activating factor 1(APAF1), inhibitors of apoptosis (IAPs), and caspases 9, 3, 6, and 7[91]. The extrinsic pathway of apoptosis is ligand dependent and is thus known as the death receptor pathway. Fas ligand binds to FAS. Induction of caspase 8 dimerization and autocleavage leads to downstream activation of executioner caspases and cell death[91]. Morphologic characteristics of cells that have undergone apoptosis include DNA fragmentation, nuclear pore formation, and increased attraction of phagocytic cells[91].

Necrosis

The uncontrolled pathway of cell death is termed necrosis. This cell death form notably causes regional damage and inflammation due to exposure of the surrounding area to the contents of the dying cell[91]. Causes of necrosis include hypoxia and inflammation[91].

Necroptosis

In 2005, a form of cell death exhibiting features of necrosis through a regulated induction pathway was described[100]. Necroptosis shows features similar to the extrinsic pathway of apoptosis considering the involvement of receptor-mediated cell death[98]. Necroptosis involves the phosphorylation of Mixed Linkage Kinase domain Like pseudokinase (pMLKL) with subsequent oligomerization and translocation to the cell membrane inducing pore formation, cell permeabilization, and cell death with the release of intracellular contents into the surrounding area[98]. This process is inhibited by necrostatin-1[101]. Necroptosis has been shown to be involved in cell death in response to blood toxicity suggesting a role in intracerebral hemorrhage[101].

Pyroptosis

Pyroptosis is a form of inflammatory cell death involving cleavage of caspase 1 with downstream activation of IL-1 beta[94]. Features of pyroptosis include a combination of cell death with release of inflammatory cytokines[94, 96]. This form of programmed cell death has been suggested to play a role in the pathophysiology of neurologic disease including Alzheimer's Disease and stroke[88, 102, 103]. As various neurologic conditions involve a robust inflammatory response, pyroptosis may contribute broadly to neurologic disease.

Ferroptosis

Ferroptosis was initially described in 2012 as an iron dependent non-apoptotic form of cell death[95]. This cell death pathway has been an active area of study for cancer and neurologic disease[104-109]. Early studies of this cell death pathway evolved from the discovery that erastin was capable of inducing a unique form of cell death that is modulated by intracellular iron levels and involves increases in reactive oxygen species (ROS)[95, 110]. The ferroptotic pathway involves activity of the iron-dependent enzyme lipoxygenase which promotes downstream lipid peroxidation and cell death[111-114]. Ferroptosis is inhibited by the iron chelator deferoxamine as well as by antioxidant treatment and ferrostatin 1[95]. As intracerebral hemorrhage involves the presence of both elevated iron and reactive oxygen species, the role of ferroptosis following cerebral hemorrhage is an active area of investigation[101, 104, 106].

1.4 Focused Ultrasound

In 1880 Jacques and Pierre Curie published an essential observation; in certain crystals, physical energy such as mechanical compression is converted into an electrical current[115]. The phenomenon they described is now known as the piezoelectric effect which forms the basis of ultrasound technology[116]. The possibility of altering the shape of the crystal to generate differential properties of ultrasound was demonstrated in 1935 by shaving the quartz crystal into a convex shape resulting in a focusing of the ultrasound waves to a target point[116].

Numerous parameters describe the character of both planar (unfocused) and focused ultrasound. Changing any of these parameters will result in ultrasound that exhibits distinct features[117].

Amplitude describes the pressure differential of the ultrasound. The difference between the peak pressure (or minimum pressure) and the average pressure is the amplitude[117].

Ultrasound is a mechanical pressure that has two phases a compressive phase applying a positive pressure on the target of ultrasound and a rarefactional phase imposing a negative pressure. Amplitude, described in units of decibels, is modifiable and can be manipulated by the operator to generate differential effects of ultrasound.

Ultrasound power, reported in Watts, is calculated as the square of the amplitude[117]. The power per unit area of the targeted region is termed the intensity of ultrasound and is reported as Watts/cm^2.This is the primary parameter utilized to describe the safety of ultrasound and predict resultant biological effects[117].

The biological effects of focused ultrasound were reported in the 1920s[118]. These reports described the effect of ultrasound on cells indicating the potential for ultrasound to be applied to and alter animal cells and tissues. In addition to mechanical effects induced by focused ultrasound, the biological changes in tissues subjected to focused ultrasound are dependent on factors such as thermal and neuromodulatory effects[119-124].

Thermal: Focused ultrasound has been found to induce heating in the target tissue[119, 121-123]. The heating is a result of ultrasound absorption by tissues with the conversion from mechanical energy to thermal[117]. The temperatures achieved with focused ultrasound can be of a sufficient level to cause tissue ablation. This is a component of the mechanism of focused-ultrasound tumor ablation[122].

Neuromodulation: Low frequency focused ultrasound has been found to cause alterations in neuronal activity[124, 125]. Both increases and decreases in neuronal firing have been observed following focused ultrasound. This technique has therapeutic potential to diseases involving of aberrant neuronal firing such as epilepsy[126].

1.4.1 Applications: Therapeutic

Focused ultrasound has been extensively studied for transient opening of the blood-brain barrier[127-132]. An essential regulator for maintaining the integrity of the brain, the blood-brain barrier restricts the transit of circulating components into the brain parenchyma[86]. This barrier poses a challenge for therapeutics that are targeted to the brain parenchyma restricting access from the vasculature to the brain. The safe and reversible opening of the blood brain barrier with focused ultrasound has been reproducibly achieved[128, 130]. Ultrasound generates a physical disturbance of materials. Classically gas particles within liquids are particularly susceptible to alteration under the pressure of the ultrasound beam in a process called cavitation[133]. Cavitation is defined as stable involving oscillation of the gas bubbles, or inertial involving collapse of gas bubbles sending shockwaves into surrounding material[134]. Injection of circulating microbubbles facilitates cavitation by introducing additional gaseous inclusions to the system[135, 136]. The safe reversible opening of the blood-brain barrier involves predominantly stable cavitation with limitations to parameters including peak rarefactional pressure, ultrasound intensity, and microbubble dose[129, 135, 137].

Focused ultrasound has been found to lead to an activation of microglia with parameters capable of inducing blood-brain barrier opening[129, 138, 139]. This observation led to the application of focused ultrasound for microglial priming[140, 141]. This is the idea that microglia can be prepared for a biological insult if they are first activated via the application of focused ultrasound. This is an area of investigation for diseases including Alzheimer's disease in which microglial priming may result in enhanced plaque clearance[140].

An exciting potential application for focused ultrasound is clot thrombolysis[142]. This application is quite intriguing for ischemic stroke which involves the blockage of an artery in the

brain leading to hypoperfusion and impaired function of the affected brain region[1]. Mechanical thrombolysis via endovascular surgery is an accepted treatment for ischemic stroke[10]. Focused ultrasound has been studied for stroke treatment both alone and in combination with pharmaceutical thrombolysis[143-145]. Further investigation with increasingly physiologic conditions will be required to determine and optimize the benefit of focused ultrasound application to clot lysis.

1.4.2 Applications: Disease Models

The ability to use focused ultrasound to model and study disease states dates back as far as the 1940s[146]. At Columbia University, studies by Lynn and Putnam demonstrated behavioral deficits correlating to the region exposed to focused ultrasound. They observed temporary blindness following focused ultrasound to the occipital lobe, ataxia following cerebellar focused ultrasound, and paralysis and loss of sensation following spinal cord damage via the use of focused ultrasound. At the time of the study, it was realized that this could aid in the understanding of human neurologic disease. Later studies of high intensity focused ultrasound replicated additional pathologies including neuronal destruction and lung hemorrhage[147, 148]. Animal models of disease are a key contributor to our understanding of the human condition. Focused ultrasound has been successfully applied to generate damage similar to that seen in human disease thus providing a promising system for the creation of animal models.

Chapter 2: Materials and Methods

2.1 Mouse husbandry

All experiments were conducted in accordance with IACUC and AAALAC regulations.

C57BL/6J mice (stock number 000664) were ordered from Jackson Laboratories and housed in a barrier facility for at least 72 hours prior to experiments. Mice are provided with a standard diet and water ad libitum with biweekly cage changes. Mice are on a 12-hour light-dark cycle with light from 6am-6pm. Experiments were conducted on mice age 16-20 weeks of age.

Female mice were housed together for two weeks to synchronize estrus cycles.

2.1.1 Intracardiac perfusion

Mice are given a mixture of Ketamine and Xylazine 75-95 mg/kg and 5-7 mg/kg respectively diluted in normal saline via intraperitoneal injection. Following injection mice are assessed every 5 minutes for respiration and extinction of the toe pinch reflex. Once the level of anesthesia is adequate shown by extinction of the toe pinch reflex and slowed breathing fur is removed from the chest. The transthoracic cavity is exposed, and the right atrium is clipped. A needle is inserted into the left ventricle and ice-cold saline is pumped into the circulation at a rate of 6 ml/minute. A total of 12 ml of saline are infused. For immunohistochemical analysis 12 ml of 4% paraformaldehyde are infused following the saline infusion.

2.2 Focused ultrasound Application

Prior to use lab-manufactured microbubbles are activated with 20 second alternating cycles of vacuum and decafluorobutane then mixed thoroughly for even microbubble distribution. Degassed water is inserted into the head of a 1.5 MHz ultrasound transducer ensuring that no bubbles are present. The transducer is covered with a latex membrane.

Anesthesia is induced with isoflurane at 2.75% in an induction chamber. Mice are transferred to a warming pad and placed within the stereotactic apparatus with 1.5 to 2.75% isoflurane continuously supplied via nose cone. Cranial fur is removed first with clippers then with depilatory cream. Lubricating ointment is applied to both eyes. Ultrasound gel is applied to the scalp and a chamber of degassed water is placed upon the scalp and gel with a grid placed within the degassed water chamber directly above the lambda suture.

Targeting: Ultrasound is used to image the metal grid and position the focus of the ultrasound directly above the lambda suture. Once targeting is complete the transducer is moved 5.5 mm anterior and 1.5 mm to the right of the lambda suture.

FUS-ICH 2.5: For Focused Ultrasound-Induced Intracerebral Hemorrhage at 2.5 MPa (FUS-ICH 2.5), microbubbles are introduced via tail vein immediately preceding application of focused ultrasound. Focused ultrasound is applied with a 1.5 MHz transducer, pulse length (PL) of 10,000 cycles, pulse repetition frequency (PRF) of 5 and a peak rarefactional pressure is 2500 kPa, total duration 60 seconds[149, 150]. Cavitation results are recorded during the focused ultrasound application. Once the procedure is complete, mice are placed on a warming pad as they recover from anesthesia with continuous monitoring until full recovery is achieved.

FUS-ICH 1.5: For FUS-ICH at 1.5 MPa (FUS-ICH 1.5), mice are subjected to the procedure as described for FUS-ICH 2.5 with a peak rarefactional pressure of 1500kPa rather than 2500kPa[149, 150].

FUSO: For Focused Ultrasound Only (FUSO), mice are prepared as described FUS-ICH 2.5 but no microbubbles are injected prior to the application of focused ultrasound[150].

Sham: Mice are placed in the anesthesia induction chamber with 2.75% isoflurane. Once sufficient induction of anesthesia is achieved, mice are transferred to a warming pad within a

stereotactic apparatus with continuous 1.5 to 2.75% isoflurane supplied via nose cone. Cranial fur is removed with clippers and depilatory cream. Mice are allowed to recover from anesthesia on a warming pad with continuous monitoring until full recovery is achieved[149, 150].

2.3 MRI

Induction of anesthesia is achieved with 2.5% isoflurane. Once anesthetized, mice are placed into a chamber and inserted vertically into the Bruker 9.7T Magnet. Anesthesia is maintained at 2% continuously administered via nose cone. Images are obtained using Paravision software.

T2 weighted MRI (T2W MRI): Images were acquired using the following parameters: echo time (TE) 30 ms, repetition time (TR) 2500 ms, 6 averages, 1 repetition, echo spacing 10 ms, rare factor 8, slice thickness 0.4 mm. T2 images were acquired prior to injection with gadolinium.

Gadolinium enhancement: 200 microliters of gadolinium (Omniscan) is injected into the intraperitoneal cavity of mice at least 20 minutes prior to imaging.

T1 Weighted MRI (T1W MRI): Gadolinium enhanced T1 weighted images were acquired using the following settings: TE 3ms, TR 230ms, 6 averages, 70 degree flip angle, slice thickness 0.4 mm.

2.4 Behavioral assays

Neuroscore: Mice are provided a score correlating to physical condition based upon whether they are circling, their level of motility, and general appearance. A high neuroscore correlates to a normal mouse and a low neuroscore represents a mouse with severe neurologic impairment. Circling is scored with a maximum of 4 points for no circling behavior, 3 points for spontaneous large diameter circling, 2 points for spontaneous small diameter circling, 1 point for

circling when pulled by tail, and 0 points for no movement. Motility is scored with a maximum of 3 points for a normally and actively moving mouse, 2 points for a mouse that is actively moving but with an unsteady gait, 1 point for a mouse that is reluctant to move, and 0 points for a mouse with no spontaneous movement. General appearance has a maximum score of 3 points for a normal well-groomed mouse, 2 points for a well-appearing mouse with at least 5% weight loss, 1 point for a well-groomed mouse with hunched posture, 0 points for a mouse with hunched posture and evidence of decreased grooming.

Corner Turn Test: Motor function of mice is assessed using the corner turn test. Mice are placed into a plexiglass corner with glass panes angled to 30 degrees with a .5 cm space between the two panes. Once the mouse is inserted into the corner it is observed for a turn completion. Only turns in which the mouse rears fully onto one side of the apparatus before turning are counted. The test is run for 10 trials. The corner turn test apparatus is cleaned thoroughly with ethanol between mice.

2.5 Histochemistry

2.5.1 Immunofluorescence

20-micron sections: Brains following perfusion are post fixed in 4% paraformaldehyde overnight at 4 degrees Celsius. Tissues are washed 3 times with 1X Phosphate Buffer Solution (1X PBS) then incubated in 30% sucrose for at least 24 hours prior to embedding in OCT on dry ice. Sections 20 microns in depth are achieved with a cryostat.

Slides are washed with PBS 3 times, permeabilized in blocking buffer with 0.1% triton for 30 minutes, then incubated in blocking buffer (10% NGS, 1% BSA, in PBS) for 1.5 hours at room temperature. After blocking, slides are incubated in primary antibody diluted in blocking

buffer over night at 4 degrees Celsius. Antibody concentrations and details are provided in antibody table.

Slides are washed 3 times with 1X PBS then incubated in secondary antibody and directly labeled primary antibodies for 2 hours at room temperature followed by 3 washes with 1X PBS. Hoechst stain is applied for 5 minutes (dilution, 1:1000) then slides washed 3 times with 1X PBS Mounted onto a microscope slide with mounting media and coverslip is applied.

150-micron sections: Brains following perfusion are post fixed in 4% paraformaldehyde overnight at 4 degrees Celsius. Tissues are washed 3 times with Phosphate Buffer Solution and stored in Phosphate Buffer solution prior to sectioning. Sections 150 microns in depth are achieved using a vibratome. Slices are stored in Phosphate Buffer Solution with 0.1% sodium azide until use.

Sections are stained free floating. Tissues are washed with 1X PBS 3 times and permeabilized in blocking buffer with 1% Triton for 1 hour at room temperature then incubated in blocking buffer for 2 hours at room temperature. Tissues are incubated in primary antibody diluted in blocking buffer over 48 hours. Tissues are washed 5 times for 10 minutes each then incubated in secondary antibody and directly labeled primary antibodies overnight. Brains are washed 5 times for 10 minutes each. A Hoechst stain is applied for 15 minutes (dilution, 1:1000). Sections are mounted onto a microscope slide with mounting media and coverslip is applied.

TUNEL: Terminal dUTP nick end labeling is achieved using the assay kit from Promega. Slides with 20-micron thick brain slices are washed with PBS followed by 10 minute incubation in proteinase K at room temperature. Following an additional wash with PBS, slides are incubated in equilibration buffer for 10 minutes at room temperature then incubated in reaction mixture consisting of fluorescently labeled nucleotides and the rTDT enzyme for 1 hour

at 37 degrees. The reaction is stopped with 2X SCC for 15 minutes at room temperature then washed with PBS. Immunofluorescence co-staining follows with the typical protocol described above.

To generate a positive control, the proteinase K permeabilization step is followed by incubation with DNase buffer (40mM Tris-HCL, 10mM NaCl, 6mM MgCl2, 10mM CaCl2 in deionized water) for 5 minutes and incubation with DNase (10 units) in DNase buffer.

A negative control is achieved by following the TUNEL procedure with the exclusion of the rTDT enzyme from the reaction mixture.

2.5.2 Hematoxylin and Eosin

Slides with 20-micron sections are used. Hematoxylin and Eosin (H&E) staining is performed by the Columbia University histology core.

2.6 Biochemistry

2.6.1 Western Blot

Following perfusion with ice cold saline brains are collected and dissected. The right hemisphere from 2mm-6mm anterior to lambda is collected and further dissected into medial and lateral halves. The medial portion is used for experiments. Dissected brain tissue is flash frozen in liquid nitrogen then transferred to -20 degree Celsius until lysis. Tissues lysed with Abcam cell lysis buffer with added phosphatase and protease inhibitors. Tissues are homogenized with a mechanical homogenizer. Lysates are sonicated then centrifuged at 12,000 rpm for 20 minutes at 4 degrees Celsius. The supernatant is collected into a fresh tube.

Protein from brain lysates is quantified via BCA assay and 30 micrograms of protein are prepared with Laemmli buffer with 20% beta mercaptoethanol (BME). BME is excluded from

the preparation of samples to be probed with CD68. The protein solutions are then heated at 100 degrees Celcius for 5 minutes and allowed to cool to room temperature prior to loading.

Samples are run on Novex 10-20% tris-glycine gels at 160 mV for 30 minutes followed by 120 mV for one hour.

Proteins are transferred to a PVDF membrane following membrane activation with 100% methanol for 30 seconds and equilibration in transfer buffer. Transfer is conducted at 0.3 amps for 2 hours.

Membranes are incubated in Revert total protein stain solution for 5 minutes followed by 30 seconds in Revert wash solution. Total protein staining is imaged with the Licor Odyssey system using image studio software. Membranes are then incubated in Licor blocking buffer for 1 hour at room temperature then incubated in primary antibody diluted in Licor blocking buffer overnight. Antibody dilutions are listed in the antibody table. Membranes are then washed 3 times with 1x Tris-Buffered Saline (TBS) with 0.1% Triton then incubated in Licor secondary antibody (1:10,000 dilution). Washes with 1x TBS with 0.1% Triton are removed, the membranes are placed in 1x TBS then imaged in the Licor Odyssey system.

Table 2.1: Antibody Catalogue

Antibody	Company	Catalog Number	Species	Concentration	Application
CD68	Proteintech	25747-1-AP	Rabbit	1:500	WB
CD68	BioRad	MCA1957GA	Rat	1:500	IF
Cl Casp 3	Cell Signaling	9661	Rabbit	1:1000	WB
GFAP	Aves	AB_2313547	Chicken	1:1000	IF
Iba1	Biocare	CP29013	Rabbit	1:300	IF
NeuN	Millipore	MAB3777	Mouse	1:4000	IF
pMLKL	Abcam	Ab196436	Rabbit	1:500	WB

Chapter 3: FUS-ICH at 2.5 MPa Hemorrhage and Behavior

3.1: Introduction

The understanding of human intracerebral hemorrhage relies on the study of animal models. Intracerebral hemorrhage is modeled in a number of ways including direct injection of autologous blood from a mouse's tail artery or injection of bacterial collagenase into the target region of the brain[55]. The autologous blood injection model reproduces the effects of blood toxicity within the brain as well as the mass effect[55]. The collagenase injection method induces vessel rupture through the destruction of the extracellular matrix and induces blood toxicity and the mass effect. There remains a need for additional models of intracerebral hemorrhage according to the American heart association round table discussion[61]. As hypertension is an essential risk factor for the development of intracerebral hemorrhage, the involvement of mechanical intravascular pressure in an inducible model is of interest[1]. Of specific interest within models of intracerebral hemorrhage is the induction of a dynamic hematoma that expands and resolves over time as both hematoma expansion and resolution have been observed in human intracerebral hemorrhages and are believed to contribute to human intracerebral hemorrhage pathophysiology[61].

Focused ultrasound is a technique capable of inducing transient BBB opening[128, 130]. This ability has led to numerous studies probing therapeutic benefits of FUS[127, 128, 131, 132, 142, 143]. However, FUS has been noted to cause vessel rupture at pressures above the therapeutic threshold[130]. This finding raises the possibility of utilization of focused ultrasound technology for induction of vascular damage incited by a mechanical pressure-dependent insult.

To our knowledge the Focused Ultrasound induced Intracerebral Hemorrhage (FUS-ICH) model is the first inducible pressure-dependent mouse model of intracerebral hemorrhage[149, 150].

3.2: FUS-ICH Procedure

The setup for the Focused ultrasound induced intracerebral hemorrhage mouse model involves the placement of ultrasound gel over the shaved scalp of an anesthetized mouse (Fig 3.1). A water chamber is positioned to facilitate propagation of the ultrasound. A central FUS transducer is inserted into curved focused ultrasound transducer. Once lambda suture is visualized, targeting is achieved via placement of a metal grid with ultrasound-dependent detection of the location. Once the ultrasound probe is positioned directly above the lambda suture, it is repositioned 1.5mm laterally and 5.5mm anterior. Immediately prior to sonication microbubbles are administered via tail vein injection. Focused ultrasound is applied using with a spherical single element 1.5 MHz transducer, pulse length (PL) of 10,000 cycles, pulse repetition frequency (PRF) of 5 and a peak rarefactional (negative) pressure is 2500 kPa, total duration 60 seconds[130]. Upon application of the ultrasound beam, circulating microbubbles oscillate and implode causing a microjet of fluid and increased local pressure on the blood vessel (Fig 3.1). In regions where ultrasound pressures are far above the therapeutic threshold, this causes hemorrhage.

Figure 3.1: FUS-ICH Schematic

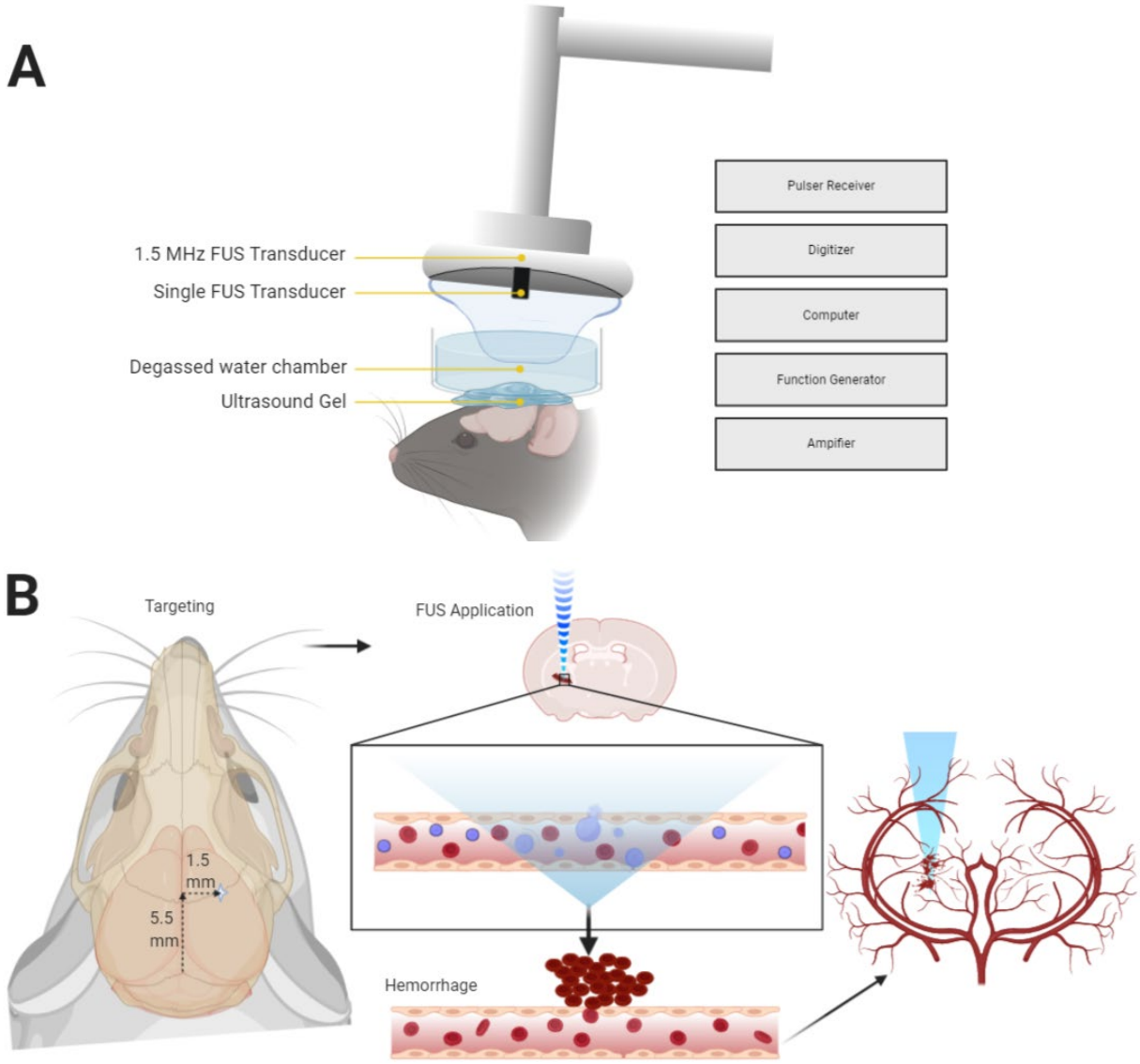

The experimental setup (**A**) of the focused ultrasound induced intracerebral hemorrhage method (FUS-ICH) involves placemen of ultrasound gel on the shaved head of an anesthetized mouse, The focused ultrasound beam travels through chambers of degassed water. The FUS-ICH procedure (**B**) involves targeting the focused ultrasound 5.5 mm anterior and 1.5 mm lateral (right) to the lambda suture observed through a shaved scalp. Under the pressure of the ultrasound beam injected circulating microbubbles oscillate and rupture sending a micro jet of fluid against the vessel wall. This causes vascular rupture and hemorrhage in vessels within the focal region of the focused ultrasound beam.

3.3: Application of FUS-ICH results in large BBB opening by 1 hour

Following FUS-ICH at 2.5 MPa (FUS-ICH 2.5), gadolinium enhanced T1 weighted MRI of the brain shows a large area of hyperintensity in the target region demonstrating gadolinium extravasation through a marked opening of the blood brain barrier (Fig 3.2). This diffuse blood brain opening is apparent as early as 1 hour following application of focused ultrasound (Fig 3.2). Notably, within the region of MRI hyperintensity are numerous hypointense sub-regions that correspond to the hemorrhage observed on post-mortem gross specimens (Fig 3.2). Although gadolinium is a contrast agent associated with hyperintensity on T1 weighted MRI, high concentrations of gadolinium have been observed to paradoxically cause regions of hypointensity[151].

The MRIs conducted on the sham mice were observed to lack both the diffuse hyperintensity seen within the sonicated hemisphere of the FUS-ICH brains and the focal regions of hypointensity (Fig 3.2). These mice demonstrate an intact blood brain barrier preventing both high- and low-level extravasation of gadolinium into the brain parenchyma. These findings are consistent among all sham mice in this study providing evidence that the blood brain barrier opening, and development of hemorrhage are a direct result of the application of the FUS-ICH technique rather than spontaneous development of pathology. Gross specimen slices of brains within the sham condition confirm the lack of hemorrhage (Fig 3.2).

Figure 3.2: Gadolinium enhanced T1 weighted MRI following FUS-ICH 2.5

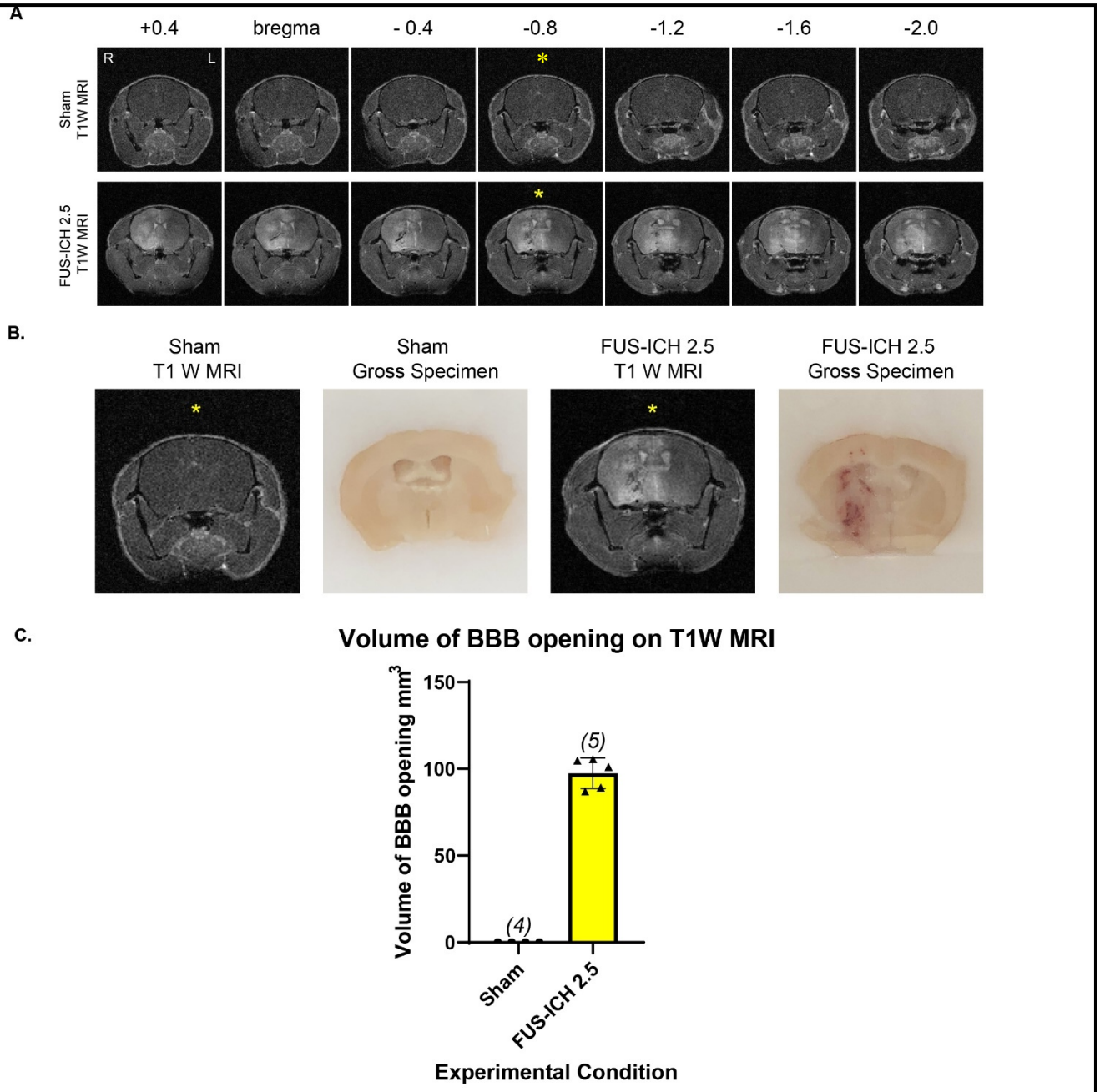

Serial T1W MRI with gadolineum (**A**) show no region of hyper-intensity in the brains of sham mice (top row). FUS-ICH mice (bottom row) show hypo-intensities within an area of hyper-intensity at 1-hour post-procedure. Key MRI images (yellow asterisk) shown enlarged (**B**) next to gross specimen images of the corresponding brain collected 24 hours post-procedure. Sham shows no hemorrhage, FUS-ICH shows hemorrhage in region corresponding to T1 hypo-intensity.

3.4: Changes apparent on T2 weighted MRI are dynamic over time

Evaluation of the T2 weighted MRI at 4 hours post-procedure demonstrates a heterogeneous region of hyperintensity within the target region (Fig 3.3). Follow-up evaluation of the same brains at 24h post-procedure shows hyperintensity on T2-weighted imaging in the corresponding region observed at 4 hours post procedure. The area of hyperintensity at 24 hours is enlarged compared to that at 4 hours (Fig 3.3). Both blood and edema may appear hyperintense on T2 weighted imaging during early timepoints following hemorrhage onset[152]. Over time the appearance of blood on MRI is anticipated to change with hyperintensity on T2 during the hyperacute or <24h timeframe with a shift toward hypointensity during the acute phase. During the hyperacute phase of FUS-ICH pathology it is difficult to distinguish hematoma from surrounding edema on T2 weighted imaging as the entire region shows hyperintensity. Gross specimen slices at corresponding locations to the MRI images demonstrate hemorrhage within the region of MRI hyperintensity, however the region of hyperintensity extends beyond the area of hematoma observable in gross specimens suggesting surrounding edema (Fig 3.3). Mice in the sham condition do not show regions of hyperintensity or hypointensity corresponding to cerebral edema or hemorrhage. Consistent with the lack of pathology apparent on T2 weighted imaging, sham mice show no signs of hemorrhage or edema on serial gross specimen slices (Fig 3.3). The gross specimen of the FUS-ICH 2.5 slices show hemorrhage through the full path of the ultrasound beam in the target region with a gradual tapering of the volume impacted by hemorrhage posterior to the target area (Fig 3.3).

Figure 3.3: T2 weighted MRI

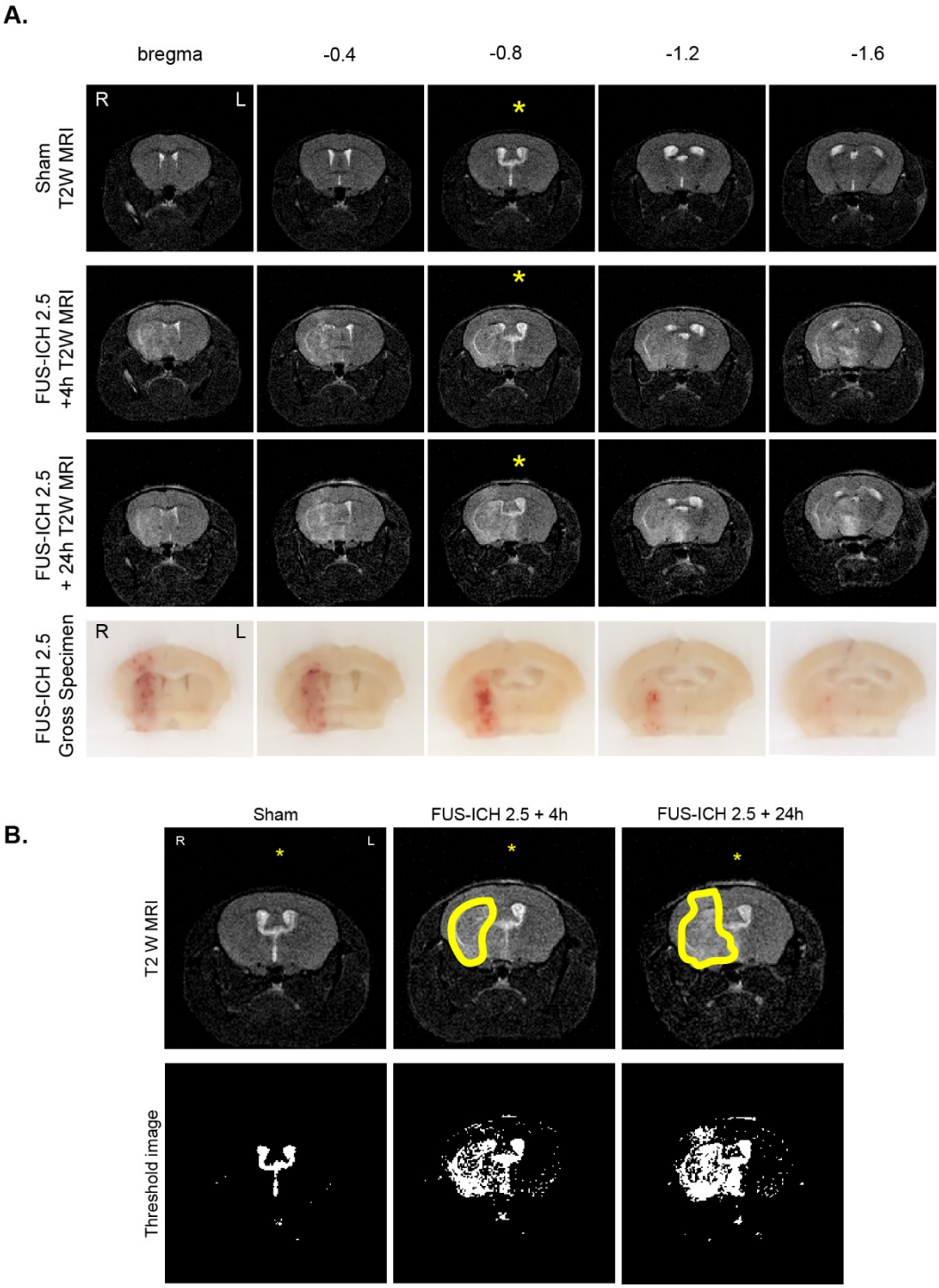

Serial T2W MRIs (**A**) of Sham (top row) and FUS-ICH 2.5 at 4 hours (row 2) and 24 hours (row 3) post-sonication. Serial gross specimen of FUS-ICH 2.5 + 24 hours (row 4) shows hemorrhage. Key sections [asterisk] are represented in (**B**) with region of hyperintensity outlined (top row) and threshold processed image showing T2W MRI Hyperintensity (bottom row).

3.5 Hematoxylin and Eosin (H&E)

Hemorrhage is apparent on H&E staining at 24 hours post FUS-ICHh 2.5 within the path of the ultrasound beam (Fig 3.4). Intact red blood cells can be observed in addition to clot formation. There is no apparent red blood cell lysis at this time. The tissue surrounding the hemorrhage does not exhibit obvious pathology (Fig 3.4).

Figure 3.4: H&E Imaging of FUS-ICH 2.5 +24 h

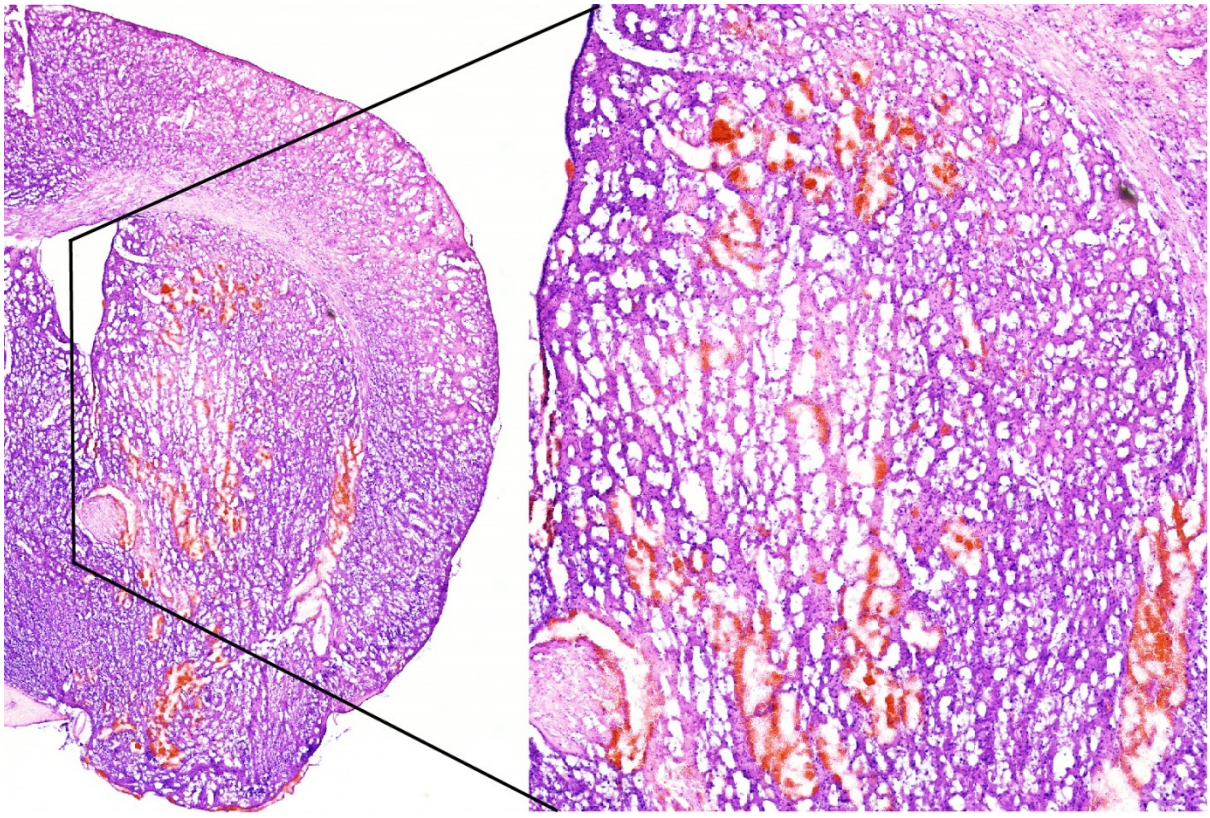

H&E imaging of a brain following FUS-ICH 2.5 at 24 hours post-sonication shows frank hemorrhage on the ipsilateral hemisphere. An enlarged image shows focal hematomas without widespread destruction to the surrounding parenchyma.

3.6: Time course

The appearance of pathology on T2 weighted MRI is dynamic following the FUS-ICH procedure. As noted above, the region of pathology appears as an area of hyperintensity at 4 hours post-procedure and appears similarly hyperintense but enlarged at 24-hours post-procedure (Fig 3.3). The properties of the blood constituting the hemorrhage changes over time resulting in distinct appearance on T2 weighted MRI imaging. During the chronic period of hemorrhage, the hematoma has been noted to appear hypointense on T2 weighted MRI. At 7 days following the FUS-ICH procedure, T2 weighted imaging shows multifocal regions of hypointensity representing hemorrhage rather than edema. At this timepoint, minimal hyperintensity is observable suggesting the resolution of edema by 7 days post-procedure within this model (Fig 3.5). Gross specimens collected 4 hours, 24 hours, and 7 days following FUS-ICH 2.5 suggest a dynamic hemorrhagic region increasing in size up to 24 hours with near-complete resolution by 7 days post-sonication (Fig 3.5). A multifocal hemorrhage is observable at 1-hour post FUS-ICH 2.5. Mice sacrificed 24 hours following the induction of intracerebral hemorrhage also show a multifocal hemorrhage but with apparent increases in red blood cell extravasation compared to 4 hours post-sonication (Fig 3.5).

The gross specimen collection is post-mortem and therefore does not allow for serial observation at distinct time points, however the appearance of the hemorrhagic region is consistent within the time points. This taken together with the dynamic size of the pathologic area on T2 weighted MRI strongly suggest the induction of a dynamic hematoma following FUS-ICH with increase in hematoma burden up to 24 hours post-procedure followed resolution to minimal pathology by 7 days post-procedure.

Figure 3.5: T2 weighted MRI and gross specimen timecourse

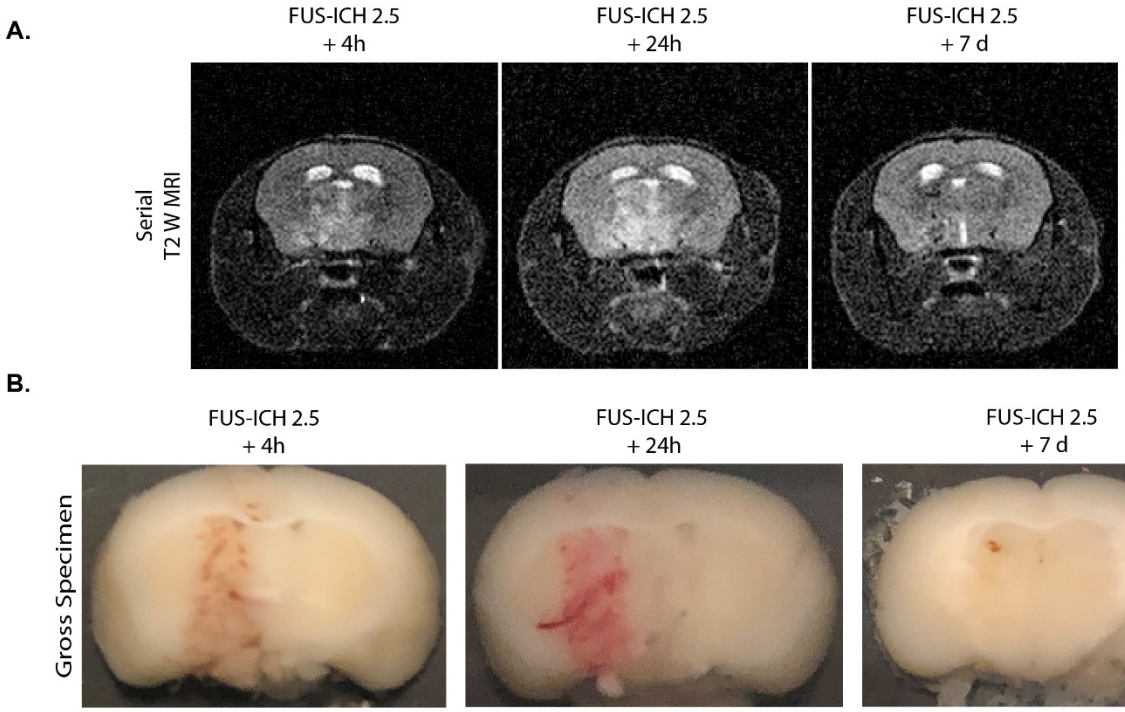

T2W MRI (**A**) of a similar coronal plane of the same FUS-ICH 2.5 -brain followed at 3 timepoints: 4 hours (left), 24 hours (middle), and 7 days (right) following sonication. Gross specimen samples from different brains collected 4 hours (left), 24 hours (middle), and 7 days (right) after FUS-ICH 2.5 procedure are shown.

3.7: Focused Ultrasound alone does not induce frank pathology

Focused ultrasound without microbubbles is capable of inducing changes in the tissue to which it is applied. The FUS-ICH model relies on the combination of high-pressure focused ultrasound with injected microbubbles. Under the pressure of the ultrasound the microbubbles oscillate creating shear stress on the vessels. At high pressures the ultrasound causes the microbubbles to become unstable and rupture causing high internal pressure on the walls of the blood vessel. It could be possible that the damage seen would arise from the pressure of the focused ultrasound and therefore be the result of pressure external to the vasculature rather than an internal pressure. To determine whether the focused ultrasound in the absence of circulating microbubbles is capable of inducing hemorrhage and damage when applied at the pressures used

for the FUS-ICH technique mice were subjected to the high pressure, 2.5 MPa, focused ultrasound in the absence of circulating microbubbles. Mice in the focused ultrasound only (FUSO) condition show no hyperintensity on T1 weighted MRI demonstrating a lack of blood brain barrier opening in the absence of circulating microbubbles (Fig 3.6). Gross specimens of the brains collected 24 hours following sonication show no hemorrhage (Fig 3.6). The lack of hemorrhage and blood brain barrier opening show that in the absence of microbubbles the focused ultrasound at 2.5 MPa does not induce the damage seen in the FUS-ICH condition. Considering this, the insult in the FUS-ICH condition is the result of the interaction between the microbubbles the focused ultrasound beam and the vasculature.

Figure 3.6: FUS Only

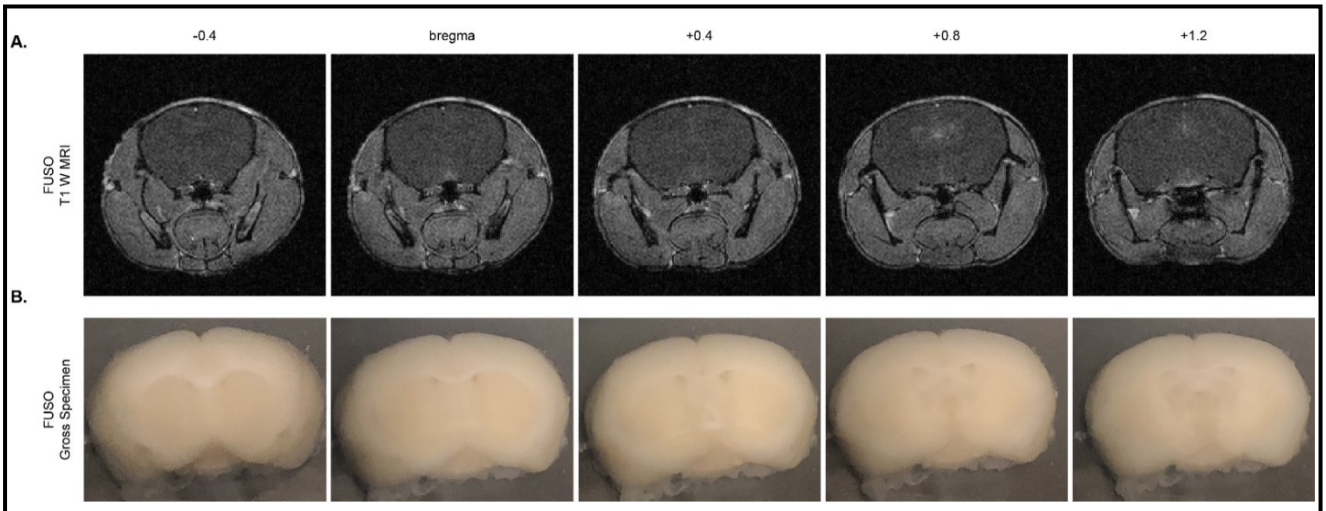

Serial T1W MRI images (**A**) of FUS O brains show no blood brain barrier opening. Serial Slices (**B**) of the same brain show no hemorrhage.

3.8 Behavioral Analysis

As the presence of lateral motor deficits is a key feature of striatal intracranial hemorrhage in humans, we employed behavioral testing to probe the presence of unilateral motor deficits in mice following FUS-ICH. Numerous testing modalities exist to analyze the behavior

of rodents in pathological conditions. A combination of a set of assays can create a reliable description of the overall neurological function of mice following insults such as stroke. The neuroscore is a multifactor assay of neurologic function often including categories such as general appearance and motility is a well-characterized neurofunctional assessment tool. Multiple distinct category combinations and scoring methods have been applied to assess the physiologic impact of neurologic disease in rodents. A 28-point neuroscore assesses many features including wire hang, grip strength, the righting reflex, and the contralateral reflex. Within this scoring system a mouse with no pathology would be expected to receive a score of 28 points whereas 0 points represents severe impairment. The studies presented here employ a restricted set of the 28-point neuroscore criteria tailored to deficits expected from a unilateral intracerebral hemorrhage. Categories included general appearance with a maximum score of 3, circling with a maximum score of 4, and motility with a maximum score of 3 are combined into a neuroscore with a maximum score of 10. In this 10-point neuroscore system, a score of 0 represents a severely impaired mouse and a score of 10 suggests no deficit.

Mice in the sham condition consistently scored 10 demonstrating no deficits in motility or general condition both on pre-procedure testing and on 24-hour follow-up (Fig 3.7). On pre-procedure testing, mice in the FUS-ICH 2.5 condition also scored consistently in the normal range with only one mouse scoring below a 10 (Fig 3.7). At 24 hours following induction of FUS-ICH, mice exhibit a variety of neuroscore results demonstrating a range of physical deficits (3.7). Mice show circling behavior, decreased motility, and changes in their overall appearance including adopting a hunched posture and decreased grooming.

Analysis of unilateral striatal damage is aided by the use of the corner turn test. The corner turn test assays the sensorimotor function of mice. Mice exhibiting a unilateral striatal

injury have been shown to develop a turning bias ipsilateral to the injury. This ipsilateral turning preference is due to weakness of the contralateral limbs impairing the mouse's ability to successfully complete turns in the contralateral direction. This assay is quite sensitive, capable of detecting a unilateral motor deficit in a mouse that appears otherwise unimpaired. Pre-procedure testing shows no bias in turning direction for both sham and FUS-ICH 2.5 mice (Fig 3.7). Sham mice continue to show no turning bias at 24-hour post-procedure testing. Mice in the FUS-ICH 2.5 group are found to demonstrate a strong ipsilateral turning bias at 24 hours post-procedure (Fig 3.7). FUSO mice were also assayed within the corner turn test apparatus to determine the presence of functional deficits despite the lack of blood brain barrier disruption and hemorrhage found in this condition. At baseline, these mice show no turning bias similar to the pre-procedure testing of the sham and FUS-ICH 2.5 conditions (Fig 3.7). Mice in the FUSO group demonstrated no turning bias compared to their pre-sonication corner turn test trials (Fig 3.7). The results of this group are similar to that of the sham mice that have undergone no focused ultrasound procedure. In absence of microbubbles the functional pathology, seen in FUS-ICH 2.5 mice as behavioral deficits in corner turn testing, are not induced.

3.9 Female mice show a more variable response to FUS-ICH

Female humans as well as mice have been shown to be less effected by intracerebral hemorrhage than males. However, females do experience intracerebral hemorrhage with substantial morbidity and mortality. For this reason, it is essential to be able to study the potential differential effects of therapeutic interventions in males and females. We set out to compare the intracerebral hemorrhage induced via the FUS-ICH method in male and female mice. T1 weighted MRI imaging of the brain following FUS-ICH 2.5 in female mice shows a diffuse region of hyperintensity within the target hemisphere with focal hypointensities as is seen in

male mice although with a possible reduction in volume (Fig 3.8). T2 weighted MRI imaging shows focal hyperintensity at both 4- and 24-hours post-sonication (Fig 3.8).

Figure 3.7: Behavioral analysis

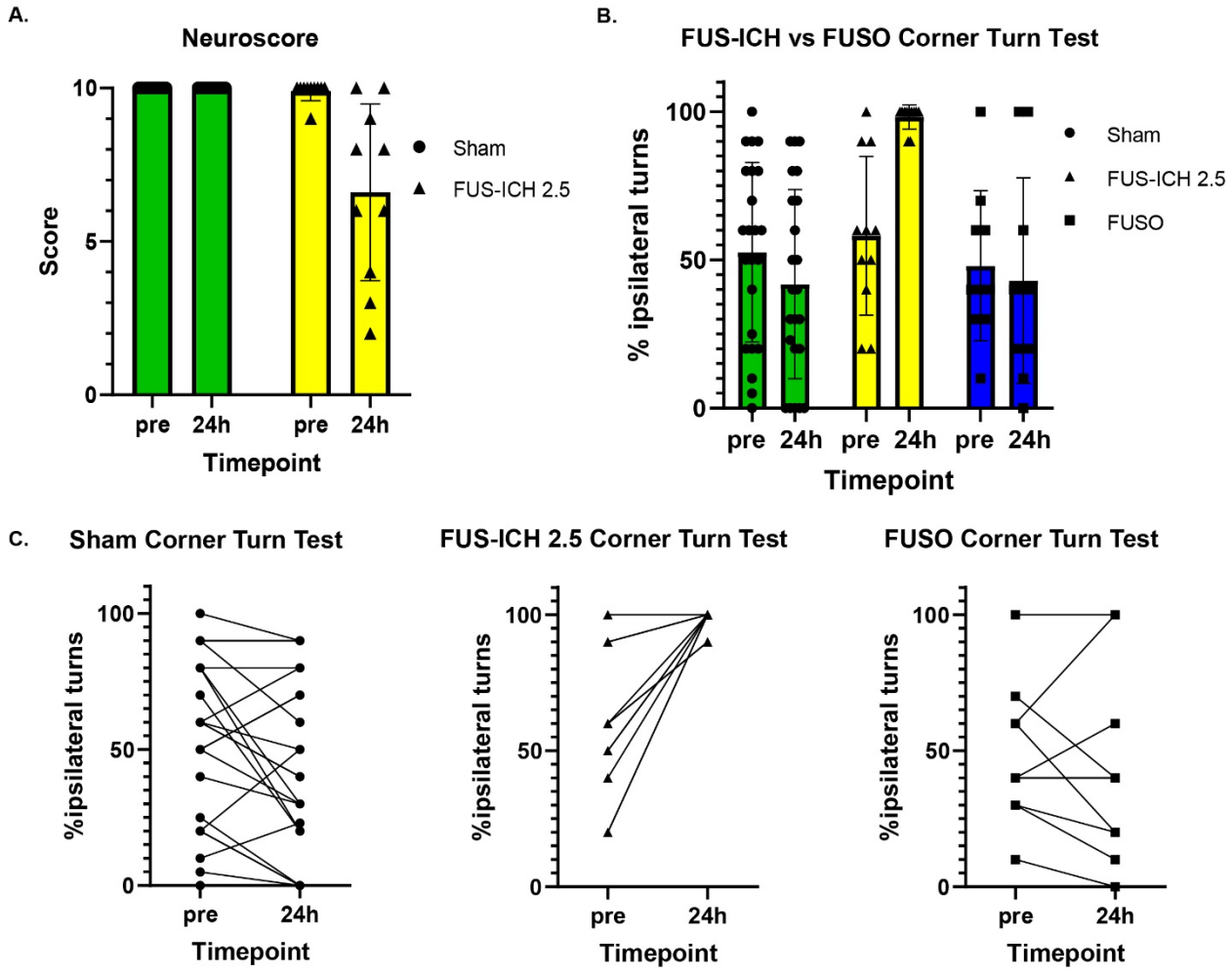

Neuroscore (**A**) comparison of Sham and FUS-ICH 2.5. Corner Turn Test Conglomerate (**B**) results for sham, FUS-ICH 2.5, and FUSO, Individual corner turn test results (**C**) are shown for sham FUS-ICH 2.5, and FUSO.

Behavioral testing shows a more variable functional response to focused ultrasound-induced intracerebral hemorrhage in females compared to males (Fig 3.8). Pre sonication corner turn testing shows no turning bias in either males or females (Fig 3.8). Corner turn test analysis shows no ipsilateral turning bias in females at either 24 hours or 7 days post-sonication (Fig 3.8).

Males in this cohort show an increase in ipsilateral turning preference by 7 days post-sonication (Fig 3.8).

Figure 3.8: FUS-ICH in female mice

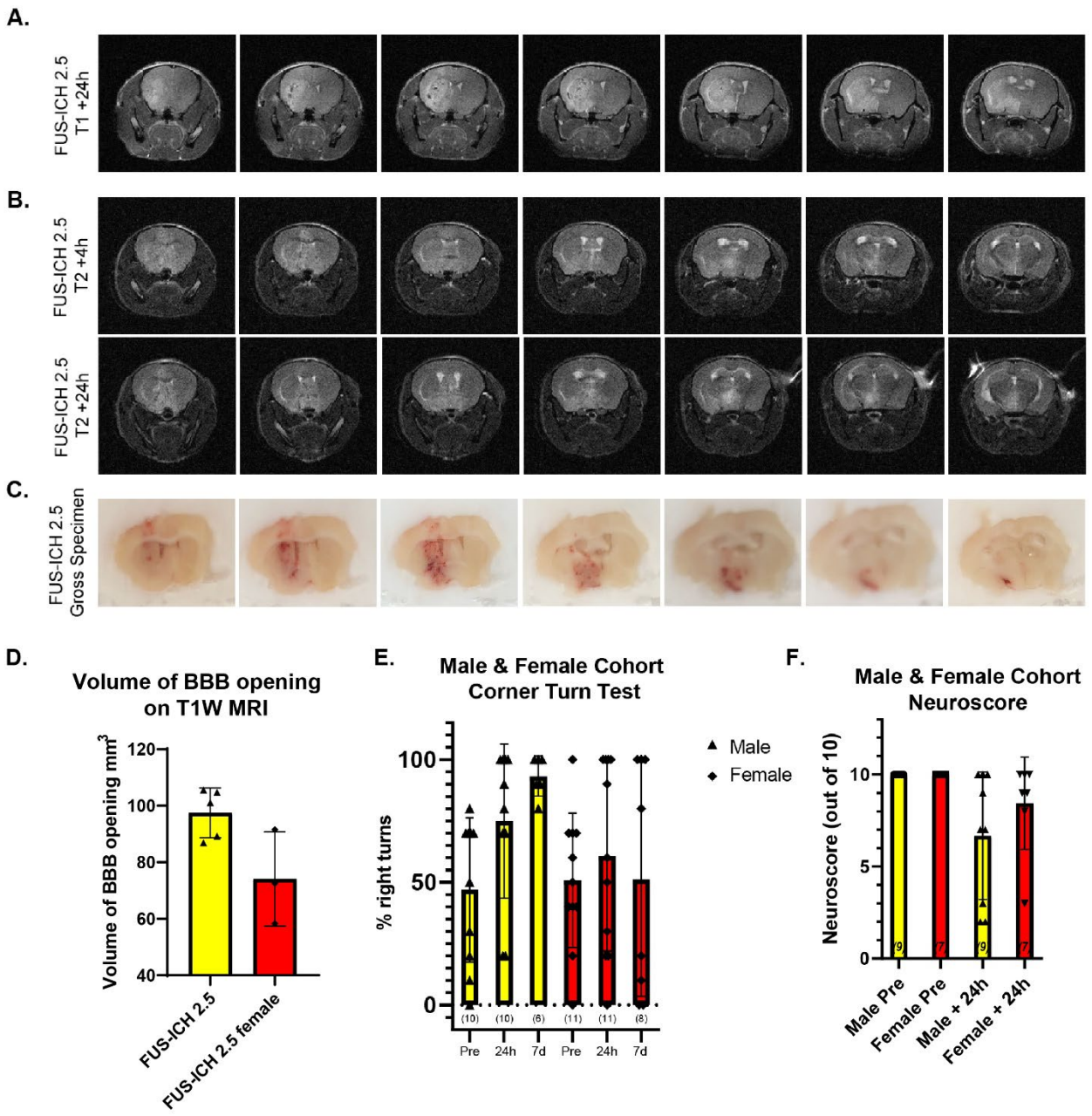

Serial T1W MRI (A) show diffuse hyperintensity and focal hypointensities with quantification (D). Serial T2W MRI (B) at 4 hours (top) and 24 hours (bottom) post sonication show hyperintensity in the ultrasound path. Gross specimen serial sections (C) show robust a multifocal hemorrhage. Corner turn test results (E) and Neuroscore (F) suggest differing outcomes compared to males.

Gross specimens show induction of a multifocal hemorrhage in the target region similar to that seen in males (Fig 3.8). Female mice do not show any apparent differences in hemorrhage induction following FUS-ICH 2.5 compared to males. Gross specimens show induction of a multifocal hemorrhage in the target region similar to that seen in males (Fig 3.8). Female mice do not show any apparent differences in hemorrhage induction following FUS-ICH 2.5 compared to males.

Using a 10-point neuroscore assessing levels of circling, motility, and general appearance also demonstrates a differential response to FUS-ICH in male and female mice. The female mice in this study show little to no deficits on the neuroscore whereas the male mice show a wide range of responses from unaffected to severely impacted (Fig 3.8).

3.10 Conclusions

The FUS-ICH technique able to generate a consistently reproducible intracerebral hemorrhage within the target region. Along the path of the ultrasound beam, vessels experiencing pressure above the pathologic threshold in combination with circulating microbubbles exhibit hemorrhage causing a multifocal hematoma involving multiple blood vessels. The hemorrhage is appreciable on both T1 and T2 weighted MRI imaging and evolves over time. The pathology induced by FUS-ICH is not replicated by application of focused ultrasound in the absence of injected microbubbles. The FUS-ICH technique induces a symptomatic intracerebral hemorrhage consistent with unilateral striatal injury. Female mice also show blood brain barrier opening and development of a multifocal hematoma following the FUS-ICH procedure however the behavioral response is more variable than the males and lateral motor deficits following the procedure in females are unable to be appreciated.

Chapter 4: FUS-ICH 2.5 Induces Cellular Responses Relevant to Intracerebral Hemorrhage

4.1 Inflammation

Inflammation is a prominent feature of neurological pathology[26, 62, 103]. In the presence of infectious processes or physical damage within the brain microglia and astrocytes mount a robust response[62, 85]. These responses also have a role in intracerebral hemorrhage pathology[26, 153]. Following blood-brain barrier disruption, the parenchymal environment is exposed to circulating immunogens that are typically shielded from brain tissues. Additionally, the blood comprising the hematoma has been found to induce neurotoxicity warranting a rapid response from the body in efforts to reestablish homeostasis[26].

Various pharmacological agents targeting inflammatory pathways are under investigation for intracerebral hemorrhage[49, 83]. As this component of intracerebral hemorrhage pathophysiology has implications for ongoing investigation in the field and the development of therapeutic agents, we set out to understand the presence and timing of inflammatory changes following FUS-ICH.

4.1.1 Morphologic changes in Iba1 following FUS-ICH 2.5

The FUS-ICH 2.5 model induces alterations in the morphology of microglia within the region of the hemorrhage compared to the sham condition (Fig 4.1). Immunofluorescence with Iba1 reveals an enlarged cell body and hypertrophied processes in the striatum at 24 hours following FUS-ICH 2.5 (Fig 4.1). Mice in the FUSO condition do not show similar changes in microglial morphology along the path of the ultrasound beam. The FUSO condition shows decreased signal intensity of Iba1 immunofluorescence (Fig 4.1). Some Iba1 can be appreciated

and shows microglia with thin processes resembling the morphology of ramified microglia (Fig 4.1).

Figure 4.1: Striatal Microglial Hypertrophy following FUS-ICH 2.5 is not seen in FUSO

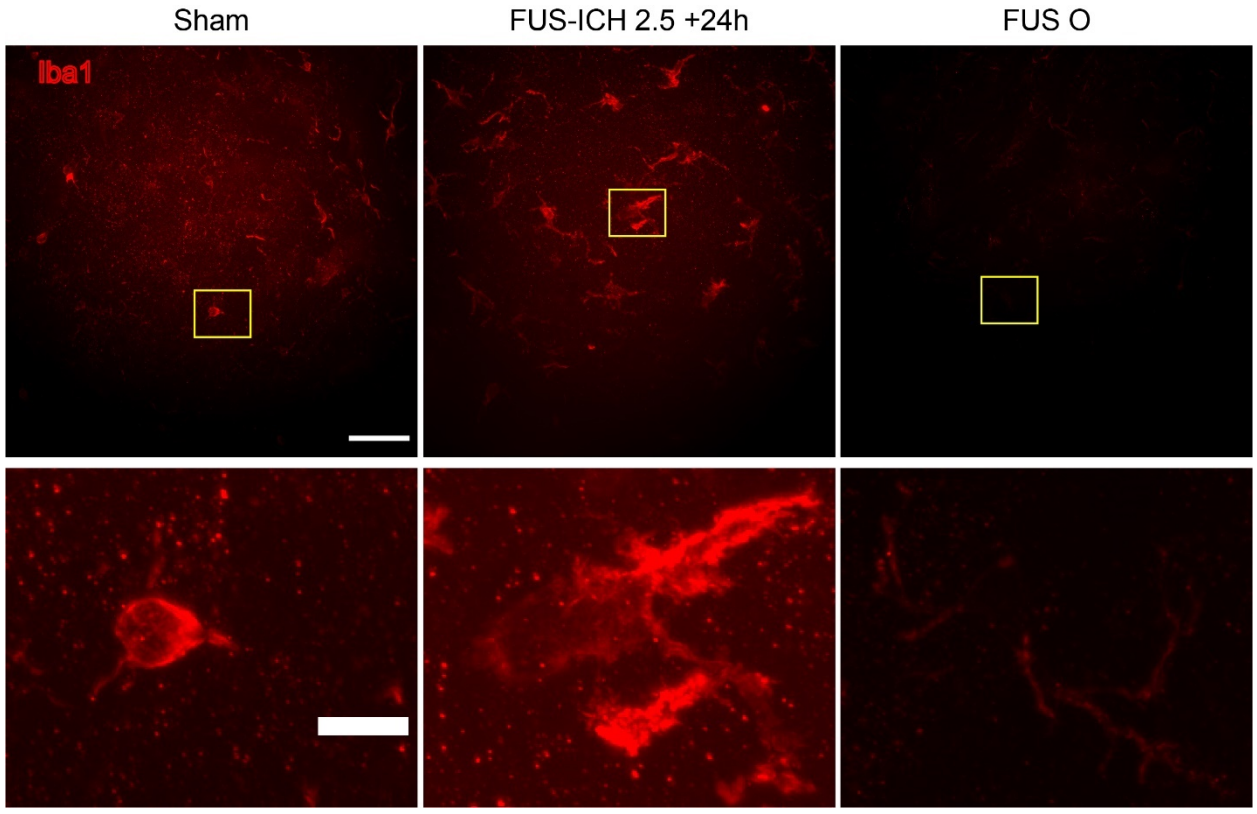

Iba1 immunofluorescence at 40x (Top) scale bar =100 microns. Yellow rectangles represent boundaries of zoomed images (bottom) scale bar =10 microns.

The timing of the onset of inflammatory changes is critical to the potential for targeting these pathways for pharmacologic intervention. Investigation of the timing of the induction of morphological changes within the microglia following FUS-ICH 2.5 demonstrate hematoma associated microglia at 1-hour post-sonication (Fig 4.2). At this timepoint the microglial morphology remains ramified with multiple branched thin processes emanating from a small cell body (Fig 4.2). At 4 hours following FUS-ICH 2.5 perihematomal Iba1 immunofluorescence shows fewer microglia processes and increased process thickness (Fig 4.2). Some microglia that

appear ramified are also present at this timepoint. As described above, microglia at 24 hours post FUS-ICH 2.5 show larger cell bodies with few hypertrophic processes (Fig 4.1). Striatal Iba1 immunofluorescence at 3 days post-sonication also shows hypertrophic microglial morphology suggesting a continued inflammatory response at this timepoint (Fig 4.2). Iba1 is not specific for microglia as macrophages are also labeled with Iba1. During homeostasis, microglia can be distinguished from macrophages morphologically as macrophages do not show microglia-like processes. However activated microglia have been shown to adopt an amoeboid morphology with retraction of processes. Therefore, the appearance of Iba1 positive cells with a large cell body and amoeboid phenotype could represent either a morphologic change in microglia or the appearance of macrophages.

Figure 4.2: Perihematomal Microglial Morphology time course

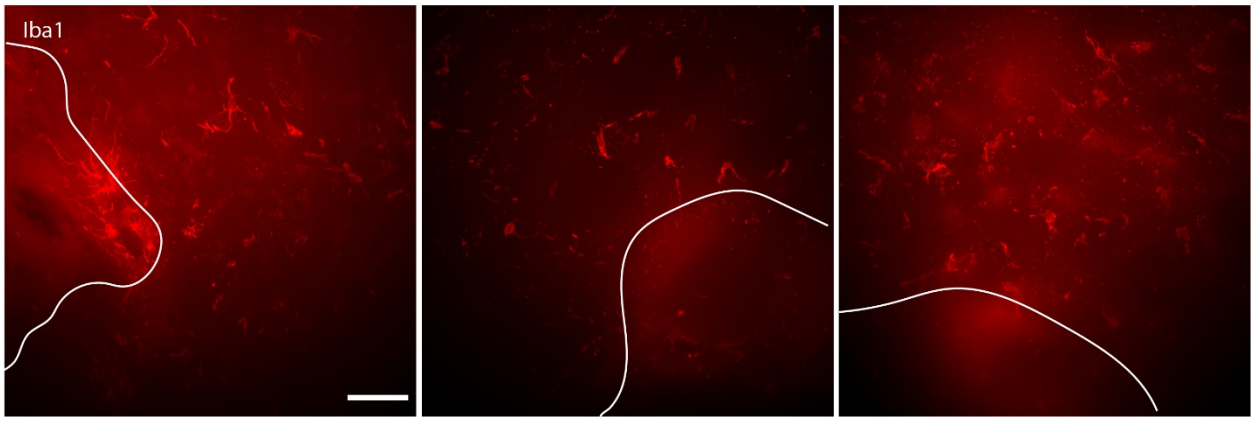

Iba1 immunofluorescence at 40x scale bar =100 microns. The white outline represents the boundaries of a hematoma.

4.1.2 Results 2: CD 68 is increased in FUS-ICH 2.5 condition up to 3 days

CD68 is utilized as a marker of the phagocytic activity of microglia and macrophages. As such, CD68 functions as a readout of microglial activation. CD68 is a glycoprotein localized to the membranes of lysosomes within microglia and macrophages. It is a member of the lysosomal

associated membrane protein (LAMP) family. The functional role of CD68 within cells is a current area of investigation.

Figure 4.3: Striatal CD68 is increased in FUS-ICH 2.5 and reduced in FUSO

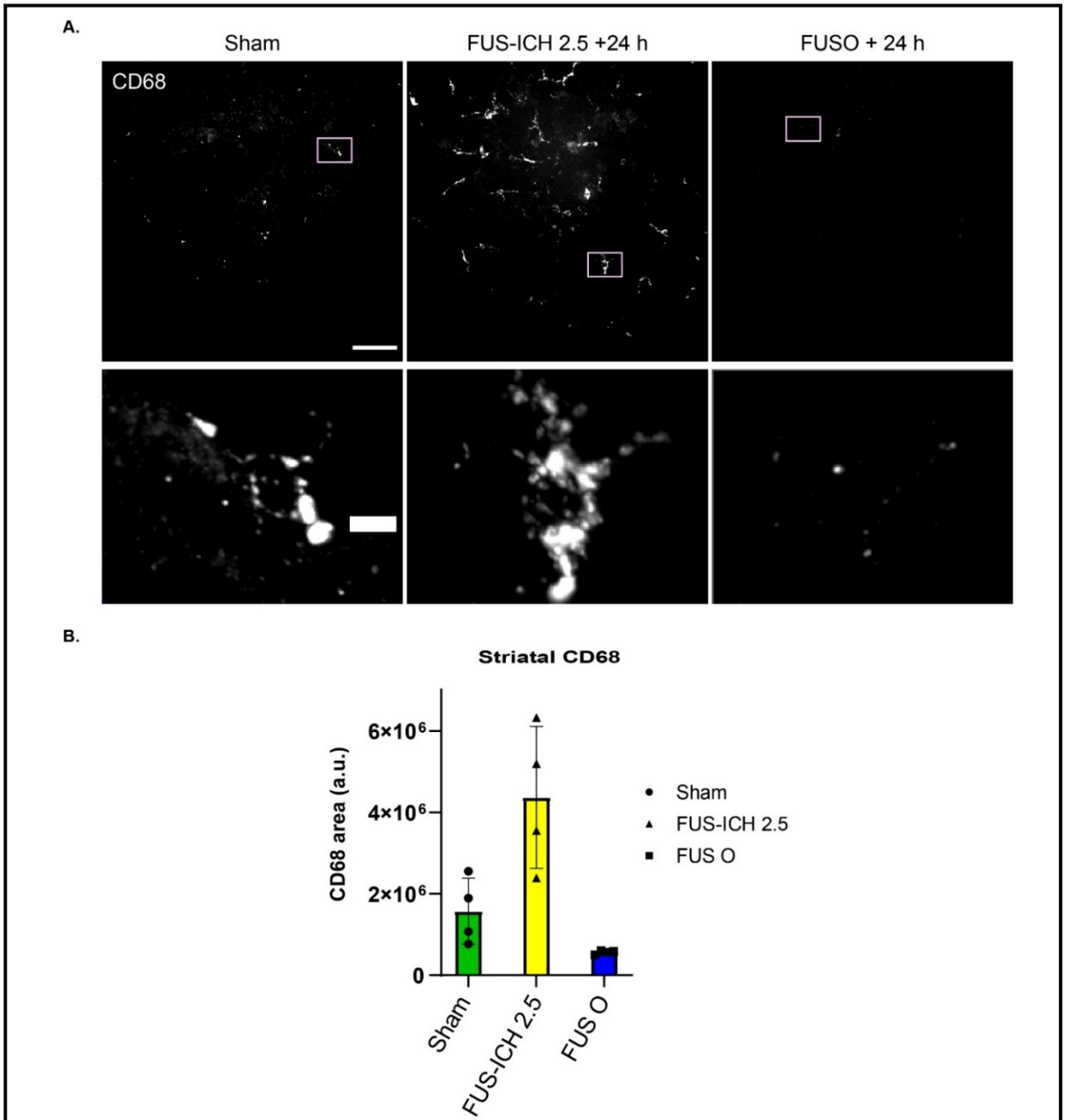

CD68 immunofluorescence (A) at 40x (top) Scale bar =100 microns, pink rectangles represent the boundaries of the zoomed images (bottom) Scale bar = 10 microns. Quantification of CD68 area (B) shows an increase in CD68 in the FUS-ICH 2.5 condition.

Homeostatic microglia exhibit a basal level of CD68 positivity with sparse puncta observable within the sham condition. There is an increase in CD68 Following FUS-ICH 2.5 within the striatum at 24 hours post-sonication (Fig 4.3). The puncta of CD68 are densely localized within the FUS-ICH 2.5 condition showing high perinuclear staining intensity. The focused ultrasound only condition does not induce an increase in CD68 within the targeted region of striatum. Intriguingly, the FUSO condition shows less CD68 positivity than the sham condition (Fig 4.3).

Figure 4.4: No difference in CD68 protein levels in Sham, FUS-ICH 2.5, and FUSO

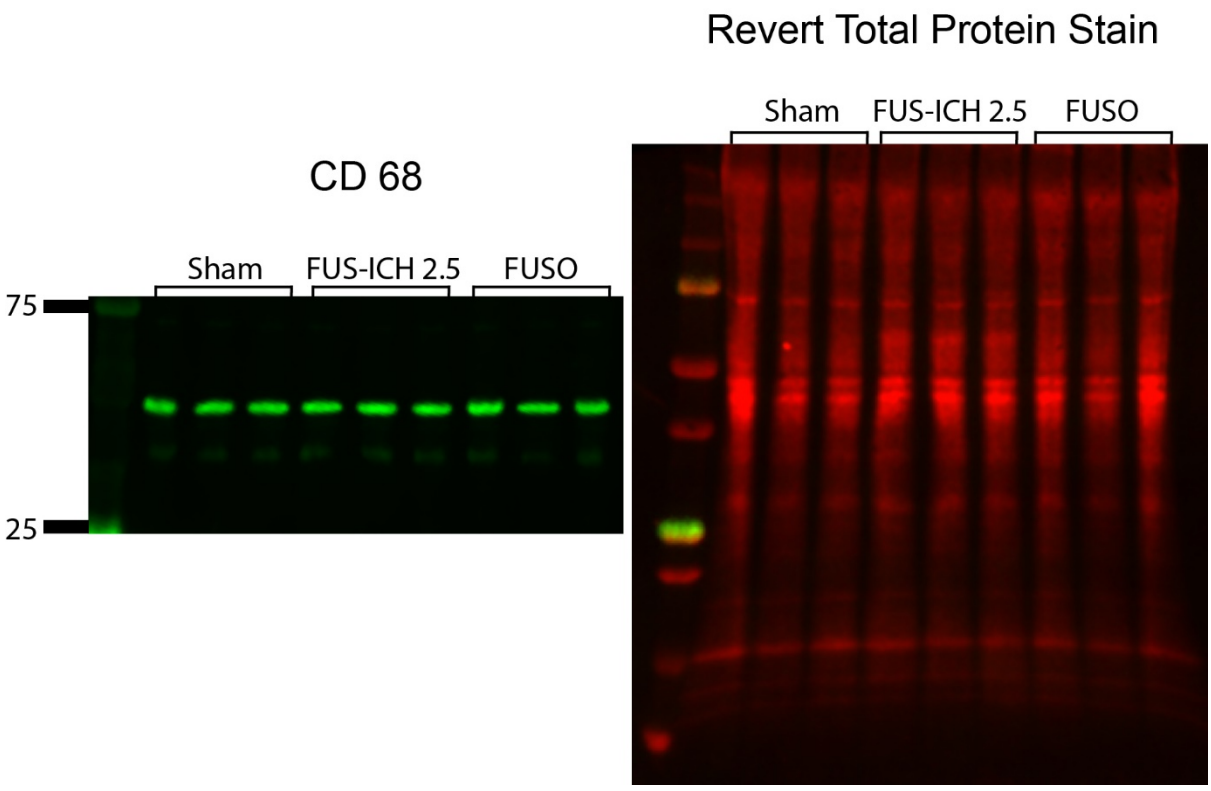

Western blot of medial right hemisphere with CD68 shows a band at approximately 40 KDa with no difference in CD68 protein levels between sham FUSO-ICH and FUSO groups. (left). The Revert Total Protein Stain shows equal loading of protein in each lane (right).

Western blot analysis of the medial half of the right hemisphere including the cortex and striatum, reveal no appreciable differences in CD68 protein levels between the Sham, FUS-ICH 2.5 + 24 hours, and FUSO conditions (Fig 4.4). Although an increase in CD68 is readily appreciated on immunofluorescence imaging of the striatum, these changes may not be sufficient to be appreciated on western blot analysis of the full medial portion of the right hemisphere.

Immunofluorescence analysis of CD68 in the FUS-ICH 2.5 condition was employed at distinct timepoints: 1 hour, 4 hours, and 3 days post-sonication. As noted above a profound difference in both the localization and the intensity of CD68 positivity are observed at 24 hours following FUS-ICH 2.5. Assessment of the timing of the onset of these changes and evaluation for resolution of the pathologic phenotype provide an understanding of the progression of inflammation within these mice. At 1-hour post-sonication, puncta of CD68 positivity are observed in an even distribution among microglial processes and cell bodies. CD68 staining intensity appears increased at 4 hours post-sonication however the distribution of the CD68 puncta remains even between the cell bodies and processes (Fig 4.5). A microglia-like morphology can be appreciated within the CD68 immunofluorescence at 1 hour and 4 hours post FUS-ICH 2.5 (Fig 4.5). The FUS-ICH 2.5 condition at 3 days following hemorrhagic induction show a marked change in the apparent localization of CD68 puncta in the perihematomal region. Intense signal positivity of CD68 is observed within the cell body with very few puncta in processes (Fig 4.5). This change in localization could indicate an alteration in the morphology of the cells present with microglia potentially retracting processes or it may represent CD68 within macrophages entering the region. Alternatively, the localization of CD68 may be altered with a loss of CD68 in the processes and concentration within the cell bodies.

Figure 4.5: Perihematomal CD68 increases up to 3 days post FUS-ICH 2.5

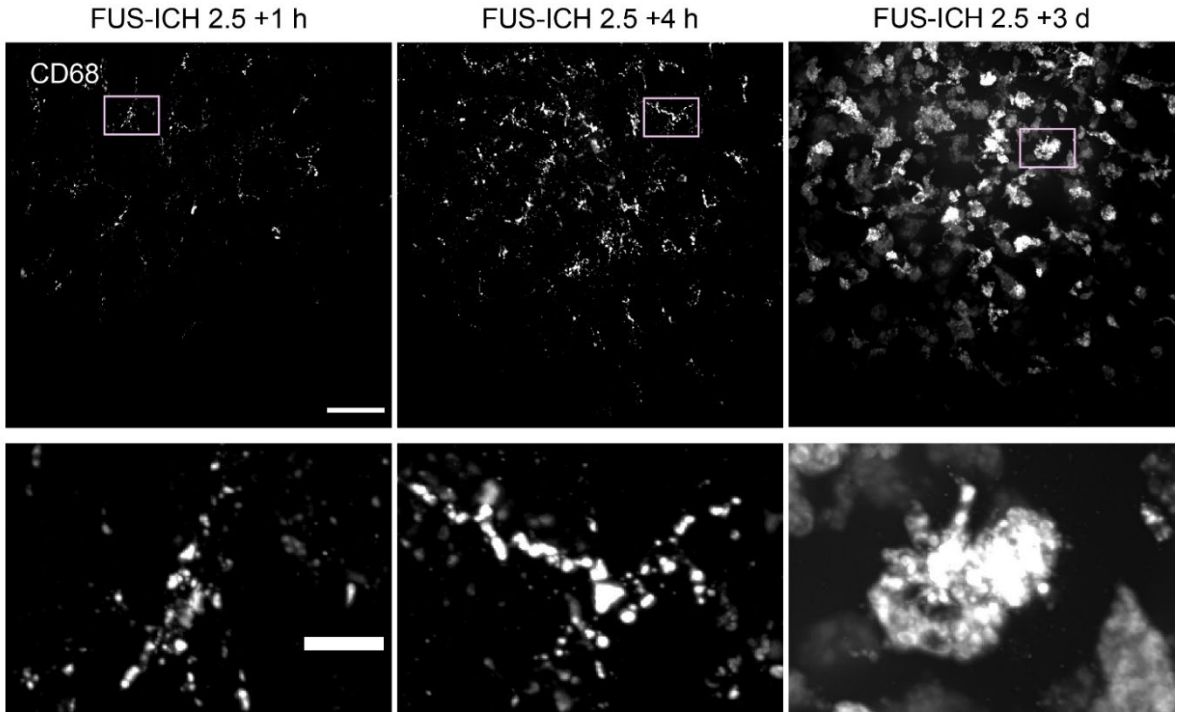

CD68 immunofluorescence at 40x (Top) scale bar =100 microns. Pink rectangles represent the boundaries of the zoomed images (bottom) scale bar =10 microns.

4.1.3 Results 3: Astrocytes show dynamic response to FUS-ICH 2.5

Astrocytes have been shown to be involved in the pathophysiology of various neurological conditions. As both a critical component of the blood-brain barrier, and a contributor to neuroinflammation, examination of the role of astrocytes in intracerebral hemorrhage is of particular interest. Glial Fibrillary Acidic Protein (GFAP) is a well-studied astrocyte marker. We employed GFAP immunofluorescence to assay the responses of astrocytes to FUS-ICH 2.5. Sham mice show robust GFAP immunofluorescence revealing stellate-shaped astrocytes (Fig 4.6). At 24 hours following induction of hemorrhage with FUS-ICH 2.5, GFAP immunofluorescence shows lower intensity than in the sham condition. Astrocyte morphology in the FUS-ICH 2.5 condition is stellate with substantial arborization (Fig 4.6). The FUSO

condition shows similar intensity of GFAP immunofluorescence to the FUS-ICH 2.5 condition. Astrocytes of the mice subjected to FUSO show increased linearity with fewer branched processes than observed in either the sham or FUS-ICH condition (Fig 4.6).

Figure 4.6: Striatal GFAP shows reduced intensity and morphologic changes in FUS-ICH and FUSO

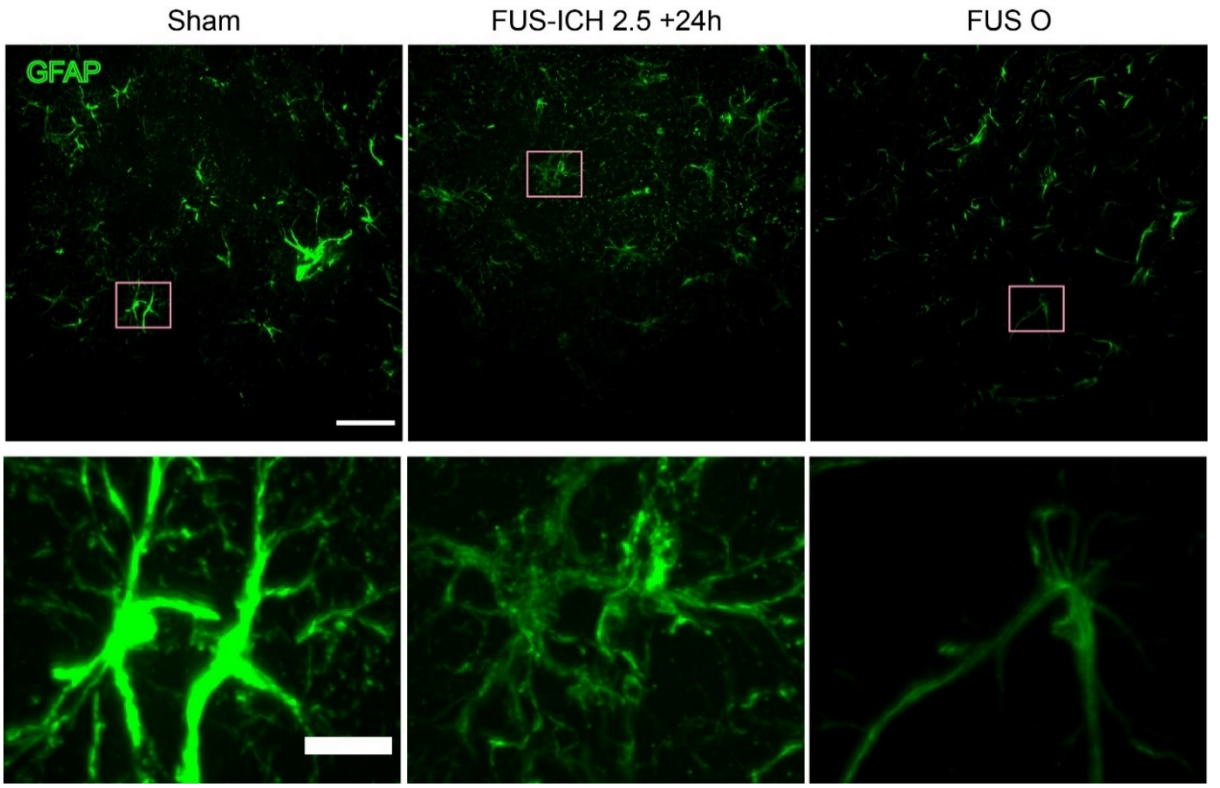

GFAP immunofluorescence at 40x (Top) scale bar =100 microns. Pink rectangles represent the boundaries of the zoomed images (bottom) scale bar =10 microns.

Time course analysis of GFAP at 1 hour, 4 hours, and 3 days following FUS-ICH induction reveals a progressive increase in GFAP signal with alterations in morphology (Fig 4.7). At 1 hour following FUS-ICH very little GFAP positivity is observable within the perihematomal region (Fig 4.7). By 4 hours post-sonication there is an increase in GFAP signal intensity compared to 1-hour post-procedure. Astrocytes with few processes are seen in the

perihematomal region. At 3 days post-induction of hemorrhage, there is a robust increase in GFAP signal intensity (Fig 4.7). Astrocyte processes appear hypertrophic. There appears to be a dynamic astrocyte response to FUS-ICH

Figure 4.7: Perihematomal GFAP is low at 1-hour post FUS-ICH with profound increase by 3 days

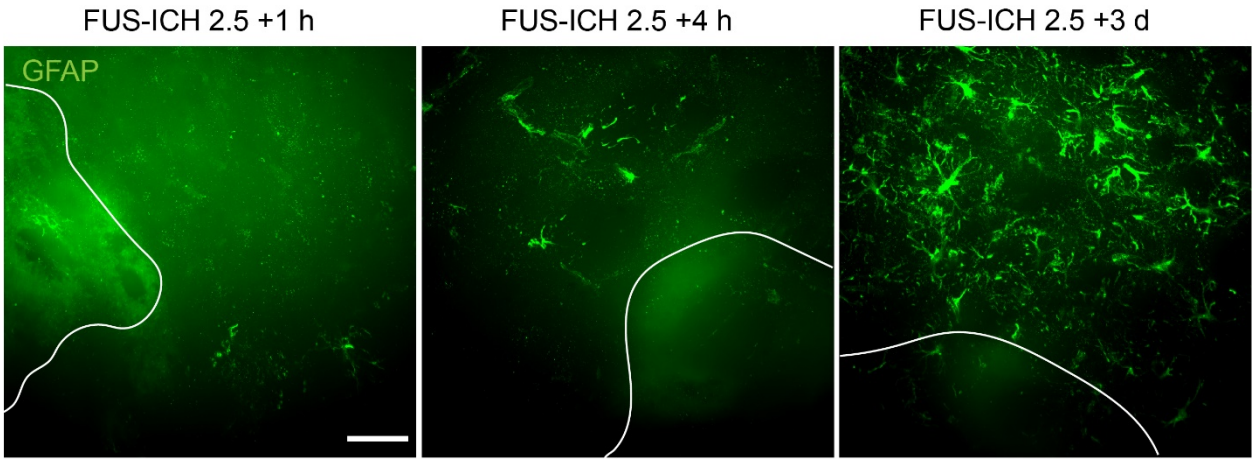

GFAP immunofluorescence at 40x scale bar =100 microns. The white outline represents the boundaries of a hematoma.

4.2 Cell death

4.2.1 The presence of cell death in FUS-ICH 2.5 is shown with TUNEL

Cell death is a critical factor of intracerebral hemorrhage pathology. TUNEL, (Terminal dUTP Nick End Labeling) is a marker of DNA fragmentation that occurs during cell death. TUNEL assays were employed to assess the presence of cell death within the FUS-ICH 2.5 condition. The TUNEL assay reveals cell death in the FUS-ICH 2.5 condition at 24 hours post procedure in the perihematomal region (Fig 4.8). Mice in the Sham condition do not show similar cell death.

Figure 4.8: TUNEL positivity in FUS-ICH 2.5 + 24h

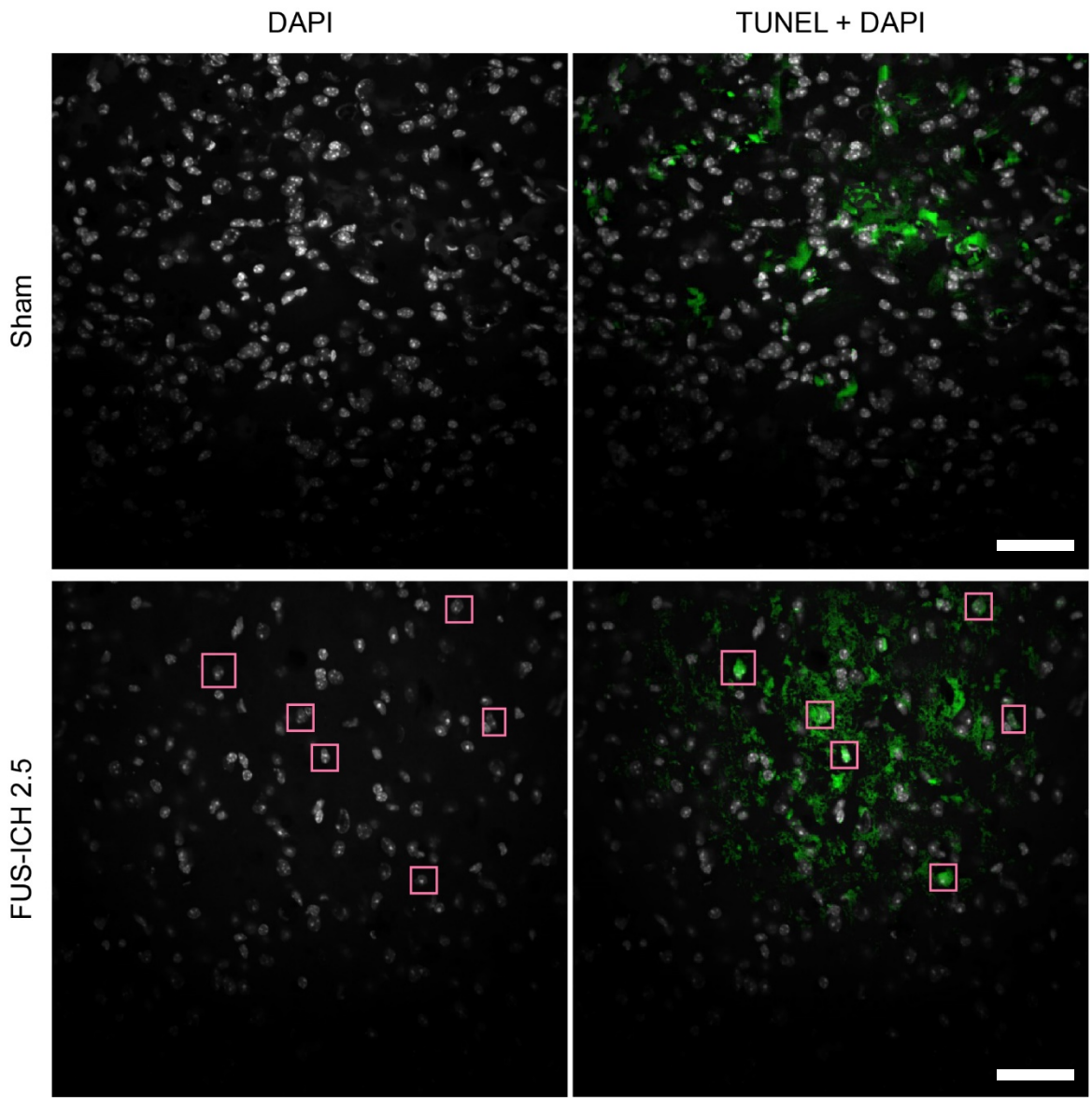

TUNEL labeling (right) in Sham (top) and FUS-ICH (bottom) show clusters of TUNEL positivity in FUS-ICH 2.5 + 24h. Co-stain with Hoechst (left) show nuclei within TUNEL positive Clusters (pink rectangles). Scale bar = 100 microns.

Markers of various cell death pathways

The evaluation of cell death pathways is an active and evolving area of study. Numerous distinct pathways to cell death have been discovered and are implicated in neurologic disease including apoptosis, necroptosis, and ferroptosis. To assess the possible contribution of the apoptotic and

necroptotic pathway to the cell death seen in the FUS-ICH 2.5 group, western blot analysis was employed probing components of distinct cell death pathways. Cleaved caspase 3 (cl casp 3) and phosphorylated MLKL (pMLKL) are used to assess the possibility of apoptosis and necroptosis following FUS-ICH 2.5. Cleaved caspase 3 originally believed to primarily function to induce cell death is now appreciated as having varied functions. The presence of cleaved caspase 3 would support the possibility of involvement of apoptosis in the FUS-ICH induced cell death but would not confirm this to be the case. All brains assayed show the presence of both pMLKL and cl casp 3 (Fig 4.9). Involvement of apoptosis and necroptosis are a possibility within this system, but further investigation will be necessary to determine the contribution of these pathways to FUS-ICH 2.5 induced cell death.

Figure 4.9: Cl casp3 and pMLKL are seen at similar levels in FUS-ICH 2.5 as Sham

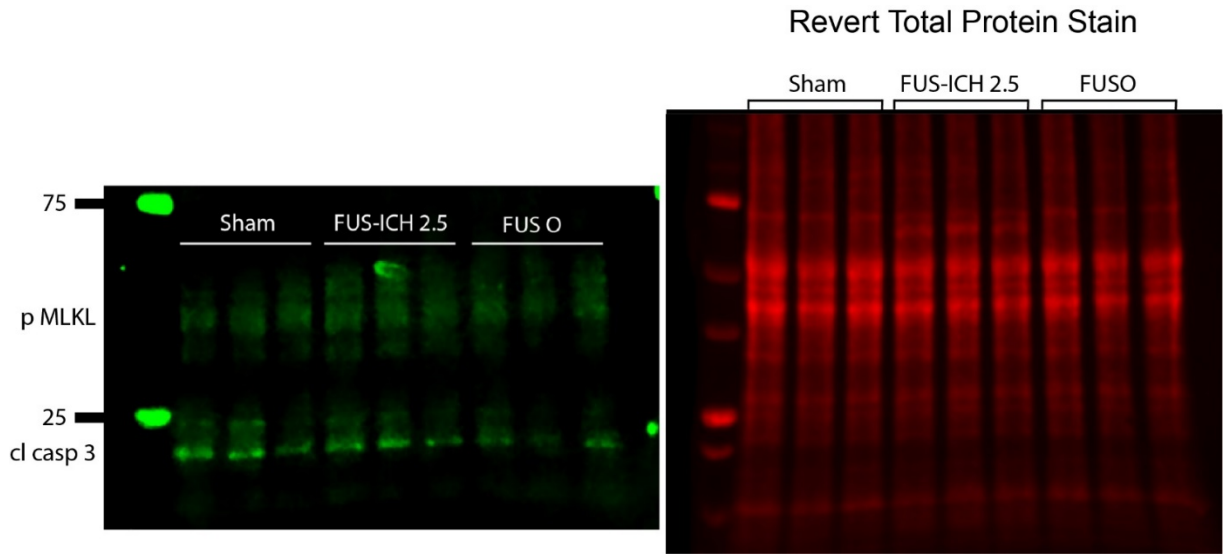

Western blot of medial right hemisphere with cl casp 3 and pMLKL show bands at approximately 20 KDa and 40 KDa respectively. Both cl Casp3 and pMLKL are observed in all conditions (left). The Revert Total Protein Stain shows equal loading of protein in each lane (right).

4.3 Conclusions

The FUS-ICH 2.5 method induces inflammation and cell death. The neuroinflammatory response to FUS-ICH includes morphologic changes in astrocytes and microglia are consistent with inflammatory activation. Microglia also show increased levels of CD68 following FUS-ICH observable by immunofluorescence. These changes are increased up to 3 days following hemorrhagic induction. Cell death is also present following FUS-ICH. Western blotting shows the presence of proteins associated with apoptosis and necroptosis, cl casp 3 and pMLKL respectively, however no conclusions can be drawn at this point as to whether cell death in the FUS-ICH condition is due to either of these pathways. Assessment of the FUSO condition does not reveal the same changes in astrocyte or microglia morphology as the FUS-ICH condition. Notably the intensity of immunofluorescence in the FUSO condition is below that seen in sham mice for both CD68 and Iba1. This suggest that the focused ultrasound alone does impact tissue morphology but is not responsible for the changes observed following FUS-ICH 2.5.

Chapter 5: FUS-ICH 1.5 MPa

5.1 Introduction

The parameters used during the application of focused ultrasound determine the resulting effects. Pressure, pulse length, and frequency have all been reported to cause varying outcomes when the parameter is altered[124, 125, 143, 154]. As pressure is the key parameter of interest in the FUS-ICH model considering the believed pressure dependency in human intracerebral hemorrhage pathology, varying the pressure applied for the FUS-ICH technique is of interest. Previous reports studying the safety of focused ultrasound for therapeutic purposes have determined that at high pressures focused ultrasound induces extravasation of red blood cells into the parenchyma[130]. The size of the extravasation has been found to be altered with changes in the pressure applied during sonication.

Human intracerebral hemorrhage pathology shows wide variability from asymptomatic cerebral microbleeds to debilitating hemorrhagic stroke[20, 51]. Clinically, cerebral microbleeds are often discovered incidentally on imaging as patients generally lack symptoms that would lead them to seek treatment. The pathophysiology is believed to involve high intravascular pressure as hypertension is a critical risk factor of cerebral microbleed development. Asymptomatic intracerebral hemorrhage is found in numerous neurological conditions including dementia and may be a predisposing factor for a large intracerebral hemorrhage or hemorrhagic stroke. Understanding of the contribution of asymptomatic intracerebral hemorrhage to the pathophysiology of other neurologic conditions remains incomplete. There exists a limited ability to model asymptomatic intracerebral hemorrhage. All of this together poses a particular need for the development of inducible mouse models of asymptomatic intracerebral hemorrhage involving high intravascular pressures.

5.2: BBB opening and Hematoma on MRI

Application of the FUS-ICH technique with the same parameters previously described for the induction of symptomatic intracerebral hemorrhage with the exception of a reduction of the peak rarefactional (negative) pressure to 1.5 MPa instead of 2.5 MPa results in blood brain barrier opening and the development of intracerebral hemorrhage (Fig 5.1, Fig 5.2)). Gadolinium enhanced T1 weighted MRI imaging shows a large, diffuse region of blood-brain barrier opening (Fig 5.1). Similar to FUS-ICH at 2.5 MPa, FUS-ICH induced at 1.5MPa shows focal regions of hypointensity within the diffuse hyperintensity corresponding to areas of substantial blood-brain barrier opening and hemorrhage (Fig 5.1). At 3 days post-sonication the same brains show a substantial reduction in the area of hyperintensity compared to that seen at 24 hours post-procedure. Only a focal hyperintensity along the path of the focused ultrasound beam is visible at 3 days following the FUS-ICH 1.5 procedure (Fig 5.1).

T2 weighted imaging at 24 hours following FUS-ICH 1.5 shows a focal region of hyperintensity corresponding to the reported appearance of acute hemorrhage with this imaging sequence (Fig 5.1). At 3 days following FUS-ICH 1.5 T2 weighted imaging appears similar to imaging conducted at 24 hours post-procedure. There is no apparent enlargement or reduction in the size of the hyperintensity seen on T2 weighted MRI at 3 days compared to 24 hours post-sonication (Fig 5.1).

Figure 5.1: FUS-ICH induces blood brain barrier opening and hemorrhage appreciable on MRI

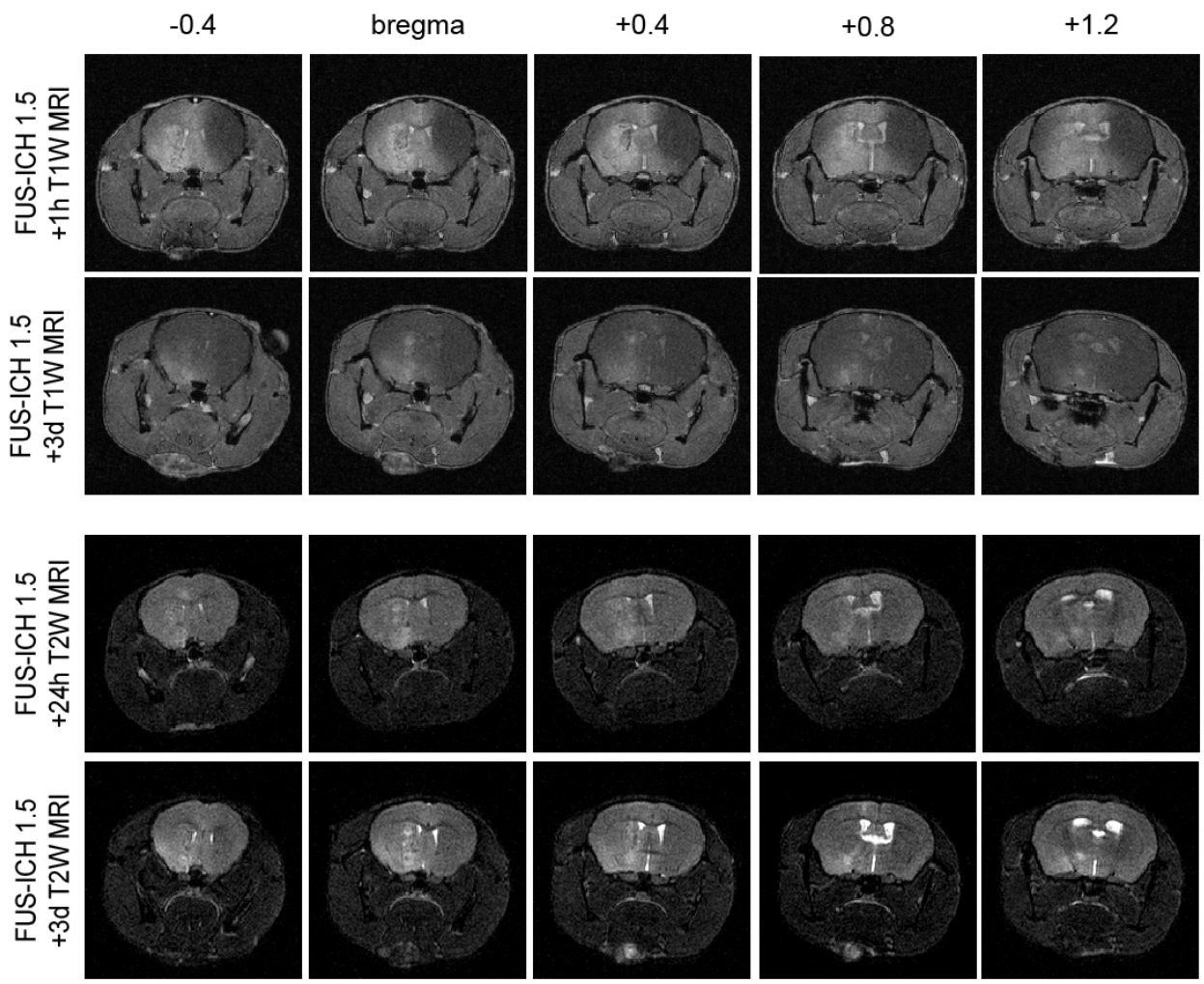

Serial T1W MRI at 1 hour post FUS-ICH 1.5 (Row 1) show diffuse hyperintensity and focal hypointensities. At 3 days post sonication T1W MRI (Row 2) shows focal hyperintensities. Serial T2W MRI at 24 hours (Row 3) shows focal hyperintensity similar to T2W MRI at 3 days post sonication (bottom).

5.3 Hemorrhage is visible on gross specimen slices

Following FUS-ICH 1.5, mice show the development of multifocal intracerebral hemorrhage within the focal region of the ultrasound beam (Fig 5.2). Consistent with reports of hemorrhage varying with pressure of focused ultrasound, the volume of brain impacted by the hemorrhage appears smaller in the FUS-ICH 1.5 condition compared to FUS-ICH 2.5. Similar to the FUS-ICH 2.5 condition, the FUS-ICH 1.5MPa procedure induces a dynamic hemorrhage with near resolution of the hematoma by 7 days post-procedure (Fig 5.2). At 4 hours following induction of intracerebral hemorrhage within the FUS-ICH 1.5 model, circular foci of hemorrhage along the path of the focused ultrasound beam are observed (Fig 5.2). FUS-ICH 1.5 shows similar multifocal hemorrhage at 24 hours with an apparent increase in the density of hemorrhagic foci within the affected region compared to 4 hours post-sonication. At 3 days post-sonication brains subjected to FUS-ICH 1.5 show the development of indentation within the hemorrhagic region suggestive of cavity formation (Fig 5.2). At 7 days following FUS-ICH 1.5, little to no appreciable hemorrhage is observed. A cavity can be observed within the sonicated hemisphere suggesting a region of resolved hemorrhage (Fig 5.2).

5.4: Behavioral analysis shows no significant deficit following FUS-ICH

To determine the presence of lateral neurological deficit in mice following FUS-ICH 1.5, the corner turn test was employed. As a sensitive assay of asymmetric motor function this test is capable of elucidating deficits that may not be appreciated on global assays of neurologic function. Both sham and FUS-ICH 1.5 mice underwent corner turn testing prior to and at 24 hours following the FUS-ICH procedure. Mice with no lateral motor or sensory deficit do not show a predictable turning bias. Individual mice may show a left turning bias or a right turning bias that is subject to change upon repeated testing however in conglomerate unimpaired mice

show no directional preference for left or right either before or after sham procedure (Fig 5.3). Mice subjected to the FUS-ICH 1.5 MPa procedure show results similar to the sham mice with no significant difference in turning bias 24 hours post-procedure compared to the pre-procedure results (Fig 5.3).

Figure 5.2: Hemorrhage is visible on gross specimen

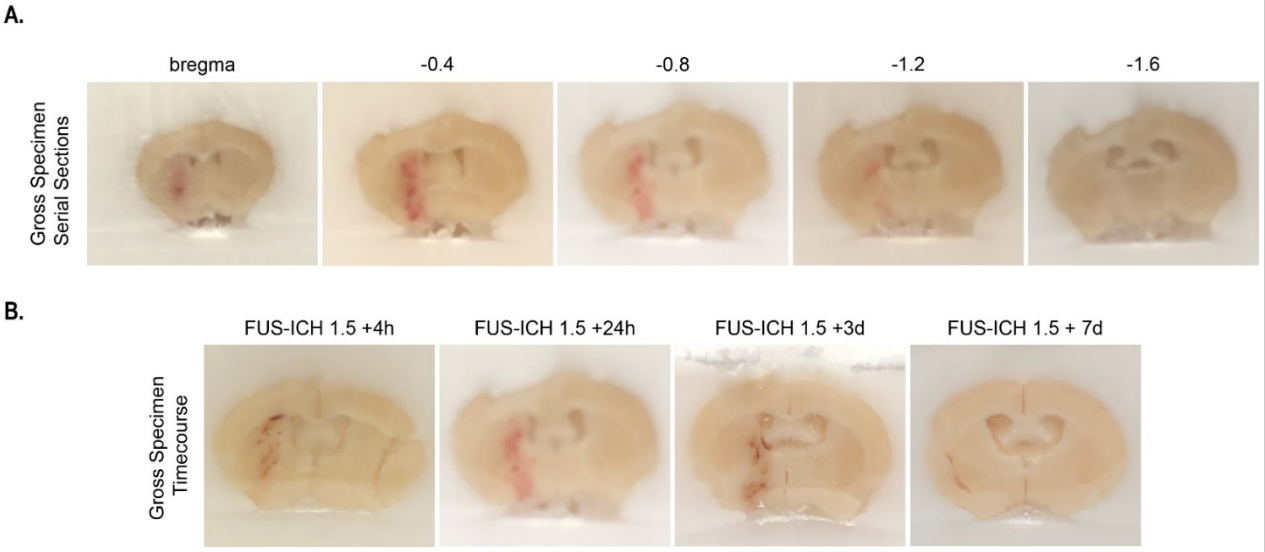

Serial sections of gross specimen (A) show a multifocal hematoma. Gross Specimen from of different brains at 4 hours, 24 hours, 3 days and 7 days post sonication following FUS-ICH 1.5 suggest changes in the hematoma over time.

To determine the presence of delayed subtle unilateral deficits the corner turn test was applied at multiple timepoints including pre, 24 hours, 48 hours, 3 days, 4 days, 5 days, 6 days, and 7 days post procedure. No significant turning bias emerged following repeated corner turn testing in the FUS-ICH 1.5MPa condition (Fig 5.3). The mice in the FUS-ICH 1.5 MPa condition do show decreased variability in turning preference and higher rates of ipsilateral turning at 4-6 days post-procedure compared to the mice in the sham condition, however this does not represent a statistically significant difference (Fig 5.3). It appears that the lack of

appreciable symptoms even with sensitive testing remains stable up to a week following FUS-ICH 1.5.

Figure 5.3: Behavioral testing reveals no lateral motor deficit following FUS-ICH 1.5

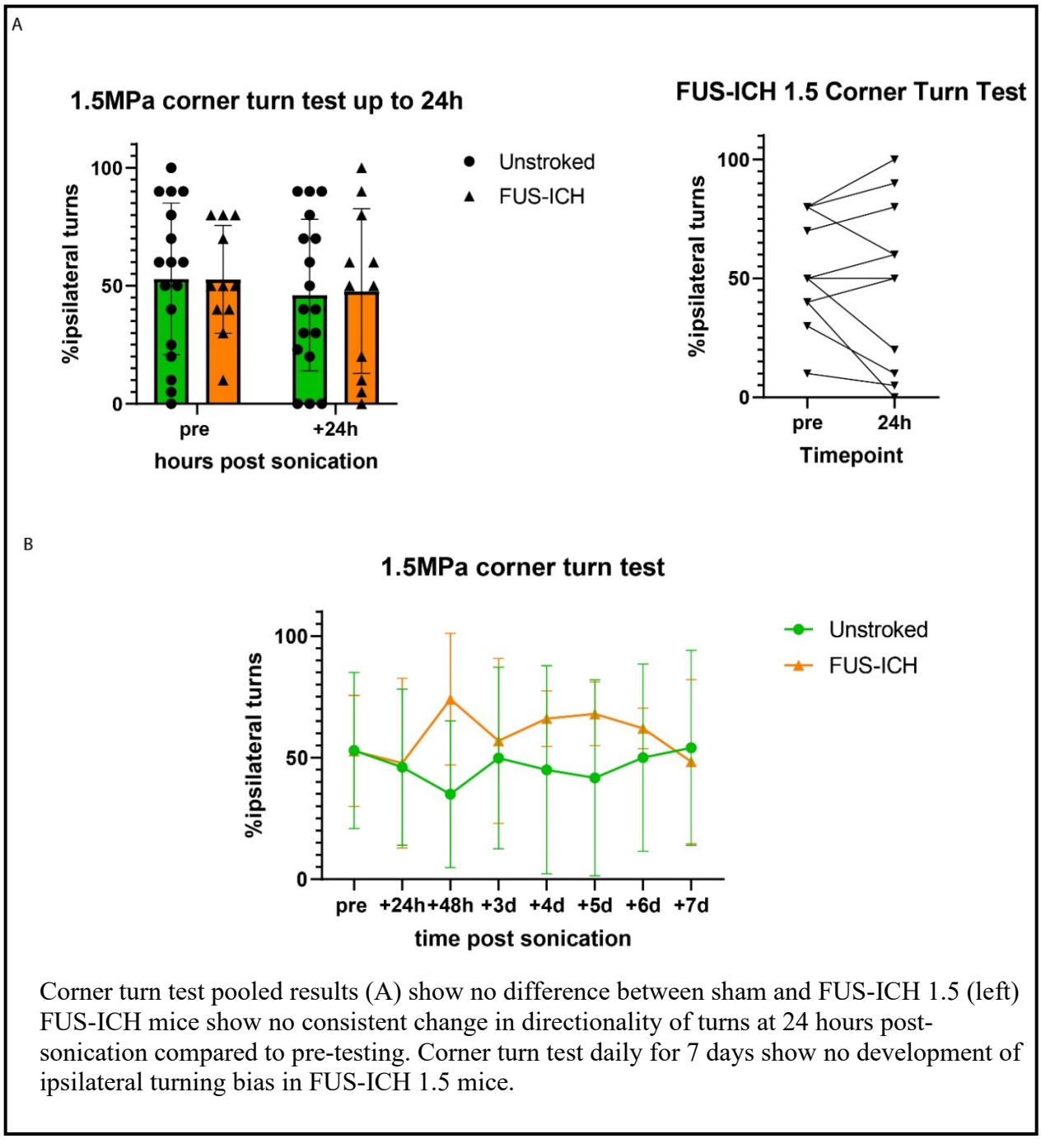

Corner turn test pooled results (A) show no difference between sham and FUS-ICH 1.5 (left) FUS-ICH mice show no consistent change in directionality of turns at 24 hours post-sonication compared to pre-testing. Corner turn test daily for 7 days show no development of ipsilateral turning bias in FUS-ICH 1.5 mice.

5.5 Inflammation is present 24 hours following FUS-ICH 1.5

As the resident immune cells of the brain, microglia are vital to the inflammatory response of neurologic states including intracerebral hemorrhage. In response to infection or pathologic insult, microglia are observed to adapt an altered morphology[72]. Following FUS-ICH 1.5 microglia are observed to demonstrate morphologic changes in the region surrounding the hemorrhagic foci. Distal to the hemorrhage, microglia are seen to exhibit a highly branched morphology with numerous long processes (Fig 5.4). In the hemorrhagic region microglia exhibit a morphology with enlarged cell bodies, and increased process thickness (Fig 5.4). These are features are associated with microglial activation suggesting a neuroinflammatory reaction to FUS-ICH 1.5 near the hemorrhage.

Figure 5.4: Iba1 morphology altered 24 h after FUS-ICH 1.5 perihematomally

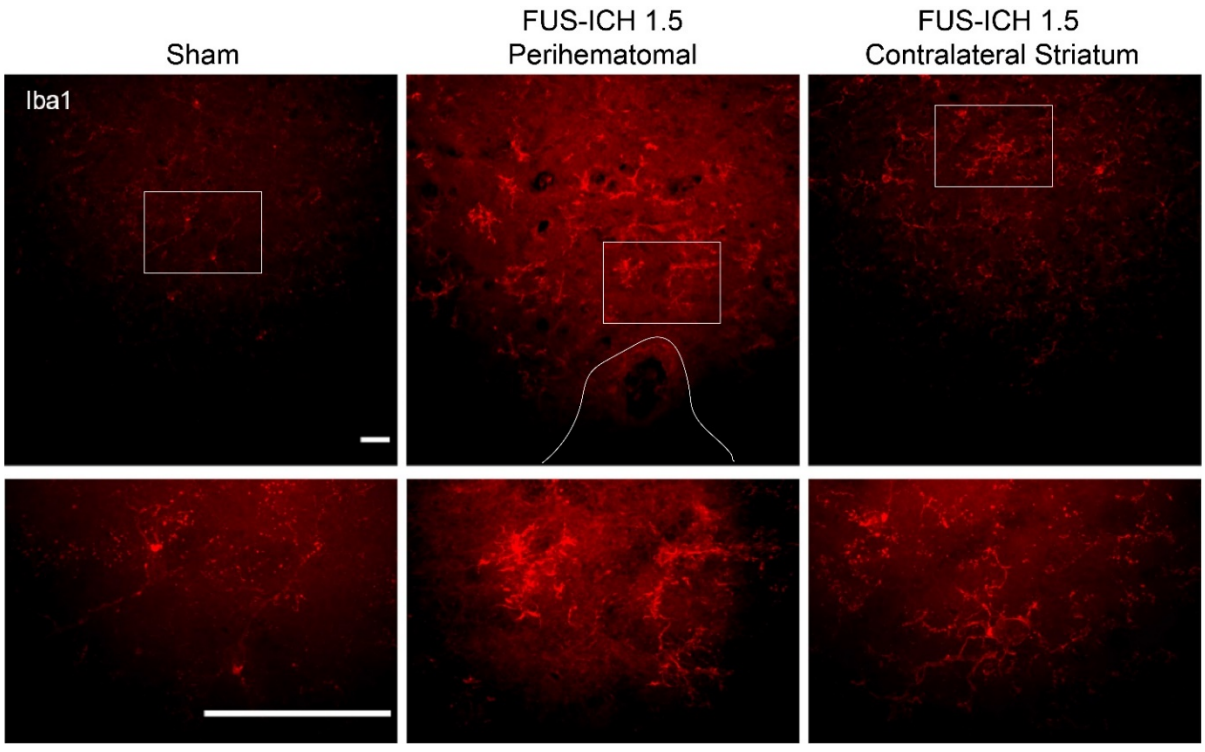

Iba1 immunofluorescence at 40x (Top) scale bar =50 microns. White outline represents the boundary of a hematoma. Rectangles represent boundaries of the zoomed images (bottom) scale bar =50 microns

5.6 No neuron loss is observed in the perihematomal striatum 24 hours following FUS-ICH 1.5

Neurons are vulnerable to neurologic insults with the loss of neurons believed to be a contributing factor to neurologic deficits in the setting of pathology. Considering this, we set out to determine whether neuron loss is apparent following the FUS-ICH 1.5 procedure. Brains of sham and FUS-ICH 1.5 mice were co-labeled with NeuN and Hoechst, markers of neurons and cell nuclei respectively. Counting of NeuN positive and Hoechst positive cells revealed no difference between the sham and FUS-ICH 1.5 conditions. Neuronal death is not appreciated within the FUS-ICH 1.5 model. Hoechst also fails to show a significant decrease in cellular density in mice flowing FUS-ICH 1.5 (Fig 5.5). Further assessment with other readouts of cell death such as TUNEL will be necessary to gain a full understanding of the presence or absence of cell death within the FUS-ICH 1.5 mode.

Figure 5.5: No reduction in NeuN positive cells following FUS-ICH 1.5 in the perihematomal region

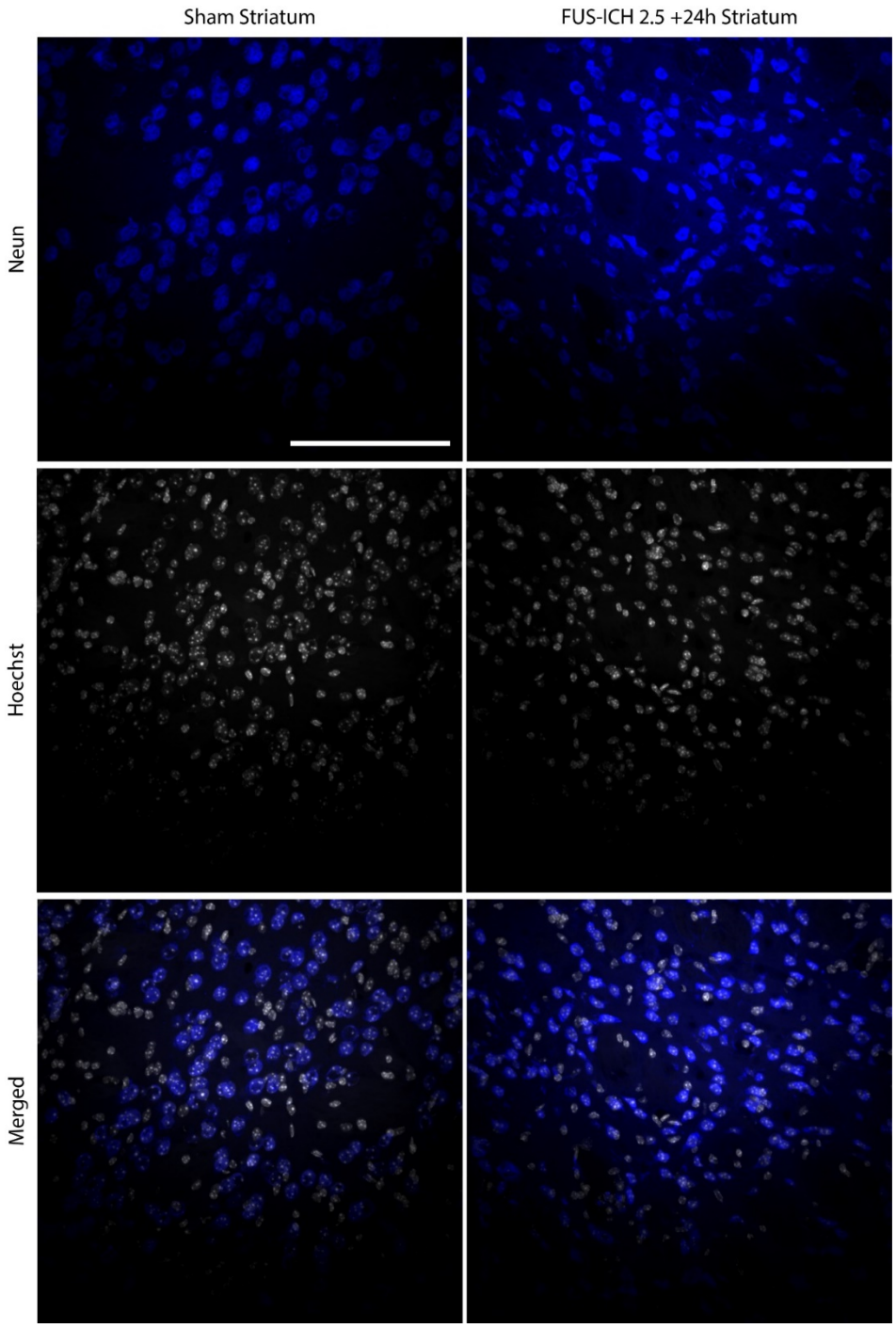

Immunofluorescence with NeuN (blue) and Hoechst (gray) at 40x scale bar=100 microns.

5.7 Conclusions

FUS-ICH 1.5 induces an asymptomatic intracerebral hemorrhage with low levels of edema and substantial hematoma resolution by 7 days post-procedure. Despite the lack of neurological deficits on behavioral testing, the brains do show signs of inflammation. This poses the possibility to use the FUS-ICH 1.5 model to better understand asymptomatic intracerebral hemorrhage and the associated contributions to other neurologic pathologies.

Chapter 6: Conclusions and Future Directions

Focused ultrasound has successfully been applied at high pressures in combination with circulating microbubbles to reliably produce mouse models of both symptomatic and asymptomatic intracerebral hemorrhage. The higher pressure FUS-ICH 2.5 condition demonstrates signs consistent with hematoma evolution including initial enlargement and subsequent resolution. Edema is appreciable on T2 weighted MRI and motor deficits are consistent with unilateral neurological damage to the striatum[155]. Behavioral testing including the neurological score and corner turn testing show clear and consistent differences between the mice in the FUS-ICH 2.5 condition and the sham or FUSO condition. These features provide the possibility of utilizing the FUS-ICH model to test potential therapeutic agents targeting intracerebral hemorrhage. Endpoints to determine efficacy of a proposed therapeutic include motor function, hematoma size, and time to resolve the hematoma. All of these features are present and modifiable within the FUS-ICH model. The primary endpoint for therapeutic discovery is functional outcome modeled by behavior as well as survival[156]. This focus has been established as the fundamental goal of applying pharmacologic agents to human disease is to modify death and disability. Pharmacologic agents have previously been tested in mice with the intention to promote resolution of the hematoma or prevent hematoma expansion but have failed to show functional benefit in clinical trials to date[47-49]. This raises the possibility that the hematoma and the size thereof is not the primary driving factor of neurologic deficits in symptomatic intracerebral hemorrhage. Considering this, it is intriguing that the FUS-ICH model generates substantial neurological deficit in mice despite not having a large focal hematoma but rather multiple dispersed hematomas. This model provides an opportunity to compare distinct

features of preclinical models to better understand other contributing factors to neurologic deficit in intracerebral hemorrhage.

Notably, neither the FUS-ICH 1.5 nor FUS-ICH 2.5 models are associated with mortality during the timeframe of this study. Mice consistently survived until sacrifice following induction of intracerebral hemorrhage. For studies intending to evaluate the pathophysiology of parenchymal hemorrhage this poses the benefit of reducing the number of mice needed to complete the study as there will be minimal loss due to mortality. The lack of mortality does however pose a limitation for studies that intend to utilize survival as an endpoint for evaluation of therapeutic efficacy. A limited 2-mouse pilot study with FUS-ICH applied at 3 MPa with all other parameters held constant has demonstrated associated mortality and increased morbidity. One mouse died within 4 hours of ICH induction while the other mouse survived but was completely immobile. The surviving mouse was also unable to support the weight of its body on the left side and therefore exhibited an unbalanced posture. Future studies will expand this pilot to generate a model of severe intracerebral hemorrhage with mortality.

The FUS-ICH technique is minimally invasive involving no craniotomy or cranial window requiring only removal of the cranial fur to allow visualization of the lambda suture through the scalp. This feature of the technique facilitates the ability to apply FUS-ICH to mice exhibiting a wide range of pathology. There is little risk of damage from the procedure itself therefore it can be applied to any mice capable of tolerating isoflurane anesthesia.

Intracerebral hemorrhage is correlated to various disease states including hypertension, diabetes, dementia[2]. In the case of dementia for example, the FUS-ICH 1.5 model can be applied to understand the role of asymptomatic intracerebral hemorrhage in mouse models of diseases such as Alzheimer's. Because the model is minimally invasive, it can be applied to aged

transgenic mice with little concern for adverse effects from the experimental setup. This study would allow for the evaluation of potential symptomatic exacerbation when intracerebral hemorrhage is superimposed on mouse models of Alzheimer's disease.

FUS-ICH can be targeted to any region by adjusting the coordinates of the stereotactic system. Superficial and deep structures within the brain are all accessible. This allows for the evaluation of intracerebral hemorrhage applied to other regions of the brain. There may be interest in generating a cerebellar hemorrhage, occipital, motor cortex or other regional hemorrhage. All of these regions can be targeted with the FUS-ICH model.

The hemorrhage induced by both pressures the FUS-ICH technique detailed here shows distinct features from existing mouse models of intracerebral hemorrhage. The hematoma produced by the FUS-ICH techniques employed here is multifocal within the path of the ultrasound beam whereas the commonly used mouse models of intracerebral hemorrhage generate a single hematoma. In addition to providing an opportunity for comparison with existing models of intracerebral hemorrhage, this model poses a tremendous opportunity for investigating cellular and molecular changes in hemorrhage adjacent tissues.

FUS-ICH 1.5 has been shown to induce an asymptomatic multifocal intracerebral hemorrhage that can be utilized to better understand the role neurologic changes that occur following asymptomatic hemorrhage as well as explore the ways that intracerebral hemorrhage contributes to pathology in the setting of additional underlying disease. Behavioral testing demonstrates that the mice following FUS-ICH 1.5 are functionally normal. They show no significant ipsilateral turning bias on corner turn testing up to 7 days post induction of intracerebral hemorrhage. Currently the inducible model of cerebral microbleed in existence is the laser induced model involving creation of a cranial window to allow for 2 photon imaging

guided micro vessel laser ablation[60]. This technique reliably produces a highly targeted injury affecting a single blood vessel. The technique can be applied to multiple vessels to induce additional foci of microhemorrhage[59]. The laser-induced cerebral microhemorrhage technique is limited to the cortex by the need for 2 photon imaging. The FUS-ICH 1.5 model poses the potential to be a model of multifocal microhemorrhage and can be applied to any target region within the brain.

Males and females have been found to demonstrate differential responses to various pathologies. Interestingly differences between males and females are observed in stroke as well with females showing relative protection[157]. Mouse models often show similar inconsistencies between pathology in males compared to females[29]. Although the female mice subjected to the FUS-ICH 2.5 procedure do not show clear protection, there is an increased variability of their functional outcomes following intracerebral hemorrhage. Estrogen has been shown to have neuroprotective effects in animal models of numerous conditions including ischemic stroke, hemorrhagic stroke, and Alzheimer's disease[29, 158, 159]. The female mice subjected to FUS-ICH were housed together for at least 2 weeks to synchronize their estrus cycles[160]. The increased variability seen in the behavioral outcomes of female mice may represent persistent hormonal differences between the mice. This method of estrus synchronization is not exact and given results showing the protective effect of estrogen, varied estrogen levels within the cohort would be expected to generate variable neurologic outcomes. Future experiments will evaluate the phase of estrus of the female mice individually and stratify results accordingly.

The focused ultrasound alone condition was included to understand the effects of application of the high pressures of the ultrasound beam to the structures of the brain. It could be proposed that the effects seen within the FUS-ICH models are the result of high mechanical

pressure of the ultrasound rather than the interaction between the microbubbles and the ultrasound resulting in increased intravascular pressure and vessel rupture. It is also possible that even in the absence of blood brain barrier opening and hemorrhage that the focused ultrasound alone would be sufficient to cause behavioral changes. For these reasons it was critical to include a focused ultrasound only condition to better understand the contribution of the individual elements of the FUS-ICH procedure to observed pathology. The FUSO condition resulted in no blood brain barrier opening or extravasation of red blood cells appreciable by MRI or gross specimen evaluation. Brains subjected to the FUSO condition showed no apparent gross pathology. Behavioral testing revealed no motor deficits with mice exhibiting normal turning preference on the corner turn test. Additionally, mice in the FUSO condition lacked cell induction of inflammatory changes. Taken together these findings support a requirement for the intravascular microbubbles for the focused ultrasound to result in the observed pathology of the FUS-ICH model.

MRI imaging of hemorrhage is complicated by the varied appearance of hemorrhage depending on the characteristics of the blood and the latency to image following the induction of hemorrhage[161]. Computed Tomography is a popular imaging modality for appreciation of intracerebral hemorrhage in humans[2]. Of particular utility is contrast enhanced CT imaging which has the ability to predict hematoma expansion using the spot sign[12]. The spot sign is a focal region of hyperdensity within the area of hemorrhage representing extravasation of contrast material thus indicating the possibility of continued hematoma growth. It is possible that the paradoxical hypointensities seen on gadolinium enhanced T1 weighted MRI following FUS-ICH represents a signal similar to the spot sign on contrast enhanced CT. These studies demonstrate a region of hypointensity within a diffuse area of hyperintensity. The diffuse hyperintensity is the

expected result in the presence of widespread blood brain barrier opening. Hypointensity has been observed in the presence of high concentrations of gadolinium[151]. High level gadolinium extravasation from the ruptured blood vessels may account the paradoxical hypointense signal. This interpretation is supported by the gross specimen slices demonstrating hemorrhagic foci corresponding to the regions of T1W MRI hypointensities.

The FUS-ICH model will join numerous mouse models of cerebrovascular disease including the models of inducible and spontaneous intracerebral hemorrhage and microhemorrhage as well as models of ischemic stroke[55, 59, 162]. The FUS-ICH 2.5 model shares key features seen in the other models of cerebrovascular disease including motor impairment, inflammation, cell death, and differential outcomes in male compared to female mice. The comparison of models of ischemic mice with models of intracerebral hemorrhage will help elucidate common key pathways in the pathophysiology of cerebrovascular disease.

6.1 Future studies of inflammation

The inflammatory changes observed following induction of FUS-ICH demonstrate a perturbation of microglia as a component of the pathophysiology. The morphological changes observed in microglia in both the FUS-ICH 1.5 MPa in addition to the increase in the lysosomal protein CD68 found in microglia and macrophages suggest a role for microglial activation following FUS-ICH. Determination of the presence of activated microglia will be further probed using RNA sequencing. Various studies have carefully detailed changes that are observed following pathology[64, 65, 69, 70]. For this reason, it will be useful to identify the presence of sequences to understand the specific changes occurring in the microglia following FUS-ICH. It will also be intriguing to compare the microglial RNA changes in the FUS-ICH 1.5 model and the FUS-ICH 2.5 model. Morphologically the two models produce distinct changes in microglia.

It is reasonable to propose that the RNA sequencing for these conditions may result in distinct populations of microglia.

The role of microglia in neurologic injury is a topic of continuous debate. There is uncertainty as to whether the microglia offer benefit or worsen pathology. Some suggest benefit in the acute setting with a transformation to pathologic prolonged inflammation in chronic disease[163]. Evidence to support each side of this discussion have been reported. Microglia are tasked with clearing debris and dead cells which is expected to be beneficial in neurologic disease however they have the capacity to release cytokines and promote prolonged inflammation which may be detrimental to the cells in the surrounding region. Future studies will evaluate the role of microglia in the FUS-ICH model. Caspase 8 has been reported to be required for microglial activation. We have an inducible conditional microglia specific caspase 8 knockout mouse line that will be utilized to explore the differences in response to the FUS-ICH procedure in mice lacking microglial caspase 8. Preliminary studies with these mice suggest a reduction in the size of the overall hemorrhage in caspase 8 knockout mice compared to controls. Further investigation will determine the necessity of caspase 8 for microglial changes associated with the FUS-ICH procedure.

6.2 Future studies of cell death

These studies demonstrated the presence of cell death following FUS-ICH 2.5 shown by the presence of TUNEL positive cells within the region of the hemorrhage. Further assessment of the cell death will be beneficial to the understanding of intracerebral hemorrhage pathophysiology. Various types of cell death have been associated with intracerebral hemorrhage[92, 101, 106]. The involvement of distinct cell death pathways will be assayed. Ferrostatin-1 and deferoxamine, inhibitors of ferroptosis, have been shown to decrease death of cultured neurons following

hemoglobin exposure[101]. Considering the involvement of iron and reactive oxygen species, there is particular interest in assaying the presence of cell death via ferroptosis in the FUS-ICH system. Currently there are no specific markers of ferroptosis so future studies will assay the possibility of this form of cell death as well as study the effects of ferroptosis prevention on outcomes in FUS-ICH mice.

References

1. Grysiewicz, R.A., K. Thomas, and D.K. Pandey, *Epidemiology of ischemic and hemorrhagic stroke: incidence, prevalence, mortality, and risk factors.* Neurol Clin, 2008. **26**(4): p. 871-95, vii.

2. Aguilar, M.I. and T.G. Brott, *Update in intracerebral hemorrhage.* Neurohospitalist, 2011. **1**(3): p. 148-59.

3. Smith, E.E., J. Rosand, and S.M. Greenberg, *Imaging of hemorrhagic stroke.* Magn Reson Imaging Clin N Am, 2006. **14**(2): p. 127-40, v.

4. Smith, E.E., J. Rosand, and S.M. Greenberg, *Hemorrhagic stroke.* Neuroimaging Clin N Am, 2005. **15**(2): p. 259-72, ix.

5. Balami, J.S., R.L. Chen, and A.M. Buchan, *Stroke syndromes and clinical management.* QJM, 2013. **106**(7): p. 607-15.

6. O'Donnell, M.J., et al., *Global and regional effects of potentially modifiable risk factors associated with acute stroke in 32 countries (INTERSTROKE): a case-control study.* Lancet, 2016. **388**(10046): p. 761-75.

7. O'Donnell, M.J., et al., *Risk factors for ischaemic and intracerebral haemorrhagic stroke in 22 countries (the INTERSTROKE study): a case-control study.* Lancet, 2010. **376**(9735): p. 112-23.

8. Zhang, Y., et al., *Lifestyle factors on the risks of ischemic and hemorrhagic stroke.* Arch Intern Med, 2011. **171**(20): p. 1811-8.

9. National Institute of Neurological, D. and P.A.S.S.G. Stroke rt, *Tissue plasminogen activator for acute ischemic stroke.* N Engl J Med, 1995. **333**(24): p. 1581-7.

10. Gralla, J., et al., *Mechanical thrombolysis and stenting in acute ischemic stroke.* Stroke, 2012. **43**(1): p. 280-5.

11. de Andrade, J.B.C., et al., *Predicting hemorrhagic transformation in patients not submitted to reperfusion therapies.* J Stroke Cerebrovasc Dis, 2020. **29**(8): p. 104940.

12. Demchuk, A.M., et al., *Prediction of haematoma growth and outcome in patients with intracerebral haemorrhage using the CT-angiography spot sign (PREDICT): a prospective observational study.* Lancet Neurol, 2012. **11**(4): p. 307-14.

13. Paciaroni, M., et al., *Early hemorrhagic transformation of brain infarction: rate, predictive factors, and influence on clinical outcome: results of a prospective multicenter study.* Stroke, 2008. **39**(8): p. 2249-56.

14. Huang, W.Y., et al., *Association of Intracranial Hemorrhage Risk With Non-Vitamin K Antagonist Oral Anticoagulant Use vs Aspirin Use: A Systematic Review and Meta-analysis.* JAMA Neurol, 2018. **75**(12): p. 1511-1518.

15. Robinson, T.G., et al., *Applicability of ENCHANTED trial results to current acute ischemic stroke patients eligible for intravenous thrombolysis in England and Wales: Comparison with the Sentinel Stroke National Audit Programme registry.* Int J Stroke, 2019. **14**(7): p. 678-685.

16. Charbonnier, G., et al., *Intracranial Bleeding After Reperfusion Therapy in Acute Ischemic Stroke.* Front Neurol, 2020. **11**: p. 629920.

17. Dowlatshahi, D., M. O'Donnell, and M. Sharma, *Possible influence of stroke etiology on hemorrhagic transformation following thrombolysis in warfarin-treated patients.* Arch Neurol, 2010. **67**(11): p. 1413; author reply 1414.

18. Petersen, N.H., et al., *Association of Personalized Blood Pressure Targets With Hemorrhagic Transformation and Functional Outcome After Endovascular Stroke Therapy.* JAMA Neurol, 2019.

19. Chin, J.H. and N. Vora, *The global burden of neurologic diseases.* Neurology, 2014. **83**(4): p. 349-51.

20. Rincon, F. and S.A. Mayer, *The epidemiology of intracerebral hemorrhage in the United States from 1979 to 2008.* Neurocrit Care, 2013. **19**(1): p. 95-102.

21. Cusack, T.J., J.R. Carhuapoma, and W.C. Ziai, *Update on the Treatment of Spontaneous Intraparenchymal Hemorrhage: Medical and Interventional Management.* Curr Treat Options Neurol, 2018. **20**(1): p. 1.

22. Dastur, C.K. and W. Yu, *Current management of spontaneous intracerebral haemorrhage.* Stroke Vasc Neurol, 2017. **2**(1): p. 21-29.

23. Hemphill, J.C., 3rd, et al., *Guidelines for the Management of Spontaneous Intracerebral Hemorrhage: A Guideline for Healthcare Professionals From the American Heart Association/American Stroke Association.* Stroke, 2015. **46**(7): p. 2032-60.

24. Smith, S.D. and C.J. Eskey, *Hemorrhagic stroke.* Radiol Clin North Am, 2011. **49**(1): p. 27-45.

25. Hreib, K.K. *Chapter 58: Intracerebral Hemorrhage*. Neurology 2016.

26. Aronowski, J. and X. Zhao, *Molecular pathophysiology of cerebral hemorrhage: secondary brain injury.* Stroke, 2011. **42**(6): p. 1781-6.

27. Leasure, A.C., et al., *Association of Intensive Blood Pressure Reduction With Risk of Hematoma Expansion in Patients With Deep Intracerebral Hemorrhage.* JAMA Neurol, 2019.

28. Rist, P.M., et al., *Lipid levels and the risk of hemorrhagic stroke among women.* Neurology, 2019. **92**(19): p. e2286-e2294.

29. Gu, Y., et al., *Estrogen reduces iron-mediated brain edema and neuronal death.* Acta Neurochir Suppl, 2010. **106**: p. 159-62.

30. Burchell, S.R., J. Tang, and J.H. Zhang, *Hematoma Expansion Following Intracerebral Hemorrhage: Mechanisms Targeting the Coagulation Cascade and Platelet Activation.* Curr Drug Targets, 2017. **18**(12): p. 1329-1344.

31. Rindler, R.S., et al., *Neuroimaging of Intracerebral Hemorrhage.* Neurosurgery, 2020. **86**(5): p. E414-E423.

32. Cruz-Cruz, C., et al., *Survival After Ischemic and Hemorrhagic Stroke: A 4-Year Follow-Up at a Mexican Hospital.* J Stroke Cerebrovasc Dis, 2019. **28**(8): p. 2109-2114.

33. de Oliveira Manoel, A.L., *Surgery for spontaneous intracerebral hemorrhage.* Crit Care, 2020. **24**(1): p. 45.

34. Bosel, J., *Blood pressure control for acute severe ischemic and hemorrhagic stroke.* Curr Opin Crit Care, 2017. **23**(2): p. 81-86.

35. Qureshi, A.I., *Antihypertensive Treatment of Acute Cerebral Hemorrhage (ATACH): rationale and design.* Neurocrit Care, 2007. **6**(1): p. 56-66.

36. Qureshi, A.I. and Y.Y. Palesch, *Antihypertensive Treatment of Acute Cerebral Hemorrhage (ATACH) II: design, methods, and rationale.* Neurocrit Care, 2011. **15**(3): p. 559-76.

37. Morgenstern, L.B., et al., *Surgical treatment for intracerebral hemorrhage (STICH): a single-center, randomized clinical trial.* Neurology, 1998. **51**(5): p. 1359-63.

38. Goldstein, J., et al., *SCORE-IT: the Spot Sign score in restricting ICH growth horizontal line an Atach-II ancillary study.* J Vasc Interv Neurol, 2012. **5**(supp): p. 20-5.

39. Majidi, S., J.I. Suarez, and A.I. Qureshi, *Management of Acute Hypertensive Response in Intracerebral Hemorrhage Patients After ATACH-2 Trial.* Neurocrit Care, 2017. **27**(2): p. 249-258.

40. Morotti, A., et al., *Intensive Blood Pressure Reduction and Spot Sign in Intracerebral Hemorrhage: A Secondary Analysis of a Randomized Clinical Trial.* JAMA Neurol, 2017. **74**(8): p. 950-960.

41. Berthaud, J.V. and B.B. Worrall, *Can the Spot Sign Identify Who Benefits From Aggressive Blood Pressure Reduction in Intracerebral Hemorrhage?* JAMA Neurol, 2017. **74**(8): p. 905-907.

42. Balasa, A., et al., *Effects of Surgery on the 30-Day Survival Rate in Spontaneous Supratentorial Intracerebral Hemorrhage.* Brain Sci, 2020. **11**(1).

43. Kim, H.T., et al., *Surgery versus Conservative Treatment for Spontaneous Supratentorial Intracerebral Hemorrhage in Spot Sign Positive Patients.* J Korean Neurosurg Soc, 2015. **58**(4): p. 309-15.

44. Phillips, V.L., et al., *Minimally Invasive Parafascicular Surgery (MIPS) for Spontaneous Intracerebral Hemorrhage Compared to Medical Management: A Case Series Comparison for a Single Institution.* Stroke Res Treat, 2020. **2020**: p. 6503038.

45. Wu, J., et al., *Emergency surgery is an effective way to improve the outcome of severe spontaneous intracerebral hemorrhage patients on long-term oral antiplatelet therapy.* Neurosurg Rev, 2020.

46. Fouda, A.Y., et al., *Minocycline in Acute Cerebral Hemorrhage: An Early Phase Randomized Trial.* Stroke, 2017. **48**(10): p. 2885-2887.

47. Selim, M., et al., *Deferoxamine mesylate in patients with intracerebral haemorrhage (i-DEF): a multicentre, randomised, placebo-controlled, double-blind phase 2 trial.* Lancet Neurol, 2019. **18**(5): p. 428-438.

48. Yeatts, S.D., et al., *High dose deferoxamine in intracerebral hemorrhage (HI-DEF) trial: rationale, design, and methods.* Neurocrit Care, 2013. **19**(2): p. 257-66.

49. He, X.F., et al., *Deferoxamine inhibits microglial activation, attenuates blood-brain barrier disruption, rescues dendritic damage, and improves spatial memory in a mouse model of microhemorrhages.* J Neurochem, 2016. **138**(3): p. 436-47.

50. Jeerakathil, T., et al., *Cerebral microbleeds: prevalence and associations with cardiovascular risk factors in the Framingham Study.* Stroke, 2004. **35**(8): p. 1831-5.

51. Shoamanesh, A., et al., *Cerebral Microbleeds and the Effect of Intensive Blood Pressure Reduction on Hematoma Expansion and Functional Outcomes: A Secondary Analysis of the ATACH-2 Randomized Clinical Trial.* JAMA Neurol, 2018. **75**(7): p. 850-859.

52. Rosidi, N.L., et al., *Cortical microhemorrhages cause local inflammation but do not trigger widespread dendrite degeneration.* PLoS One, 2011. **6**(10): p. e26612.

53. Cordonnier, C., *Brain Microbleeds.* Practical Neurology, 2010. **10**: p. 94-100.

54. Choudhary, A. and J.A. Ibdah, *Animal models in today's translational medicine world.* Mo Med, 2013. **110**(3): p. 220-2.

55. Ma, Q., et al., *History of preclinical models of intracerebral hemorrhage.* Acta Neurochir Suppl, 2011. **111**: p. 3-8.

56. Sinar, E.J., et al., *Experimental intracerebral hemorrhage: effects of a temporary mass lesion.* J Neurosurg, 1987. **66**(4): p. 568-76.

57. Ropper, A.H. and N.T. Zervas, *Cerebral blood flow after experimental basal ganglia hemorrhage.* Ann Neurol, 1982. **11**(3): p. 266-71.

58. Rosenberg, G.A., et al., *Collagenase-induced intracerebral hemorrhage in rats.* Stroke, 1990. **21**(5): p. 801-7.

59. Shih, A.Y., et al., *Rodent Models of Cerebral Microinfarct and Microhemorrhage.* Stroke, 2018. **49**(3): p. 803-810.

60. Nishimura, N., et al., *Targeted insult to subsurface cortical blood vessels using ultrashort laser pulses: three models of stroke.* Nat Methods, 2006. **3**(2): p. 99-108.

61. Hemorrhagic Stroke Academia Industry Roundtable, P., *Basic and Translational Research in Intracerebral Hemorrhage: Limitations, Priorities, and Recommendations.* Stroke, 2018. **49**(5): p. 1308-1314.

62. Baufeld, C., et al., *Differential contribution of microglia and monocytes in neurodegenerative diseases.* J Neural Transm (Vienna), 2018. **125**(5): p. 809-826.

63. Cho, K. and G.E. Choi, *Microglia: Physiological Functions Revealed through Morphological Profiles.* Folia Biol (Praha), 2017. **63**(3): p. 85-90.

64. Hanisch, U.K. and H. Kettenmann, *Microglia: active sensor and versatile effector cells in the normal and pathologic brain.* Nat Neurosci, 2007. **10**(11): p. 1387-94.

65. Chistiakov, D.A., et al., *CD68/macrosialin: not just a histochemical marker.* Lab Invest, 2017. **97**(1): p. 4-13.

66. Cherry, J.D., et al., *Microglial neuroinflammation contributes to tau accumulation in chronic traumatic encephalopathy.* Acta Neuropathol Commun, 2016. **4**(1): p. 112.

67. Friedman, B.A., et al., *Diverse Brain Myeloid Expression Profiles Reveal Distinct Microglial Activation States and Aspects of Alzheimer's Disease Not Evident in Mouse Models.* Cell Rep, 2018. **22**(3): p. 832-847.

68. Hammond, T.R., et al., *Single-Cell RNA Sequencing of Microglia throughout the Mouse Lifespan and in the Injured Brain Reveals Complex Cell-State Changes.* Immunity, 2019. **50**(1): p. 253-271 e6.

69. Lewis, N.D., et al., *RNA sequencing of microglia and monocyte-derived macrophages from mice with experimental autoimmune encephalomyelitis illustrates a changing phenotype with disease course.* J Neuroimmunol, 2014. **277**(1-2): p. 26-38.

70. Pulido-Salgado, M., et al., *RNA-Seq transcriptomic profiling of primary murine microglia treated with LPS or LPS + IFNgamma.* Sci Rep, 2018. **8**(1): p. 16096.

71. Deczkowska, A., et al., *Disease-Associated Microglia: A Universal Immune Sensor of Neurodegeneration.* Cell, 2018. **173**(5): p. 1073-1081.

72. Kreutzberg, G.W., *Microglia: a sensor for pathological events in the CNS.* Trends Neurosci, 1996. **19**(8): p. 312-8.

73. Amici, S.A., J. Dong, and M. Guerau-de-Arellano, *Molecular Mechanisms Modulating the Phenotype of Macrophages and Microglia.* Front Immunol, 2017. **8**: p. 1520.

74. Wang, J., et al., *Treatment targets for M2 microglia polarization in ischemic stroke.* Biomed Pharmacother, 2018. **105**: p. 518-525.

75. Li, Q., et al., *Developmental Heterogeneity of Microglia and Brain Myeloid Cells Revealed by Deep Single-Cell RNA Sequencing.* Neuron, 2019. **101**(2): p. 207-223 e10.

76. Burguillos, M.A., et al., *Caspase signalling controls microglia activation and neurotoxicity.* Nature, 2011. **472**(7343): p. 319-24.

77. Wang, J., *Preclinical and clinical research on inflammation after intracerebral hemorrhage.* Prog Neurobiol, 2010. **92**(4): p. 463-77.

78. Wagner, K., et al., *Inhibition of granulocyte-macrophage colony-stimulating factor receptor function by a splice variant of the common beta-receptor subunit.* Blood, 2001. **98**(9): p. 2689-96.

79. Kokona, D., et al., *Colony-stimulating factor 1 receptor inhibition prevents disruption of the blood-retina barrier during chronic inflammation.* J Neuroinflammation, 2018. **15**(1): p. 340.

80. Li, M., et al., *Colony stimulating factor 1 receptor inhibition eliminates microglia and attenuates brain injury after intracerebral hemorrhage.* J Cereb Blood Flow Metab, 2017. **37**(7): p. 2383-2395.

81. Son, Y., et al., *Inhibition of Colony-Stimulating Factor 1 Receptor by PLX3397 Prevents Amyloid Beta Pathology and Rescues Dopaminergic Signaling in Aging 5xFAD Mice.* Int J Mol Sci, 2020. **21**(15).

82. Tschoe, C., et al., *Neuroinflammation after Intracerebral Hemorrhage and Potential Therapeutic Targets.* J Stroke, 2020. **22**(1): p. 29-46.

83. Dai, S., et al., *Minocycline attenuates brain injury and iron overload after intracerebral hemorrhage in aged female rats.* Neurobiol Dis, 2019. **126**: p. 76-84.

84. Kim, H., et al., *Effect of Pioglitazone on Perihematomal Edema in Intracerebral Hemorrhage Mouse Model by Regulating NLRP3 Expression and Energy Metabolism.* J Korean Neurosurg Soc, 2020. **63**(6): p. 689-697.

85. Ding, Z.B., et al., *Astrocytes: a double-edged sword in neurodegenerative diseases.* Neural Regen Res, 2021. **16**(9): p. 1702-1710.

86. Daneman, R. and A. Prat, *The blood-brain barrier.* Cold Spring Harb Perspect Biol, 2015. **7**(1): p. a020412.

87. Allnoch, L., W. Baumgartner, and F. Hansmann, *Impact of Astrocyte Depletion upon Inflammation and Demyelination in a Murine Animal Model of Multiple Sclerosis.* Int J Mol Sci, 2019. **20**(16).

88. Sekerdag, E., I. Solaroglu, and Y. Gursoy-Ozdemir, *Cell Death Mechanisms in Stroke and Novel Molecular and Cellular Treatment Options.* Curr Neuropharmacol, 2018. **16**(9): p. 1396-1415.

89. Liddelow, S.A. and B.A. Barres, *Reactive Astrocytes: Production, Function, and Therapeutic Potential.* Immunity, 2017. **46**(6): p. 957-967.

90. Zhou, B., Y.X. Zuo, and R.T. Jiang, *Astrocyte morphology: Diversity, plasticity, and role in neurological diseases.* CNS Neurosci Ther, 2019. **25**(6): p. 665-673.

91. Elmore, S., *Apoptosis: a review of programmed cell death.* Toxicol Pathol, 2007. **35**(4): p. 495-516.

92. Bobinger, T., et al., *Programmed Cell Death after Intracerebral Hemorrhage.* Curr Neuropharmacol, 2018. **16**(9): p. 1267-1281.

93. Fink, S.L. and B.T. Cookson, *Apoptosis, pyroptosis, and necrosis: mechanistic description of dead and dying eukaryotic cells.* Infect Immun, 2005. **73**(4): p. 1907-16.

94. Brough, D. and N.J. Rothwell, *Caspase-1-dependent processing of pro-interleukin-1beta is cytosolic and precedes cell death.* J Cell Sci, 2007. **120**(Pt 5): p. 772-81.

95. Dixon, S.J., et al., *Ferroptosis: an iron-dependent form of nonapoptotic cell death.* Cell, 2012. **149**(5): p. 1060-72.

96. Fernandes-Alnemri, T., et al., *The pyroptosome: a supramolecular assembly of ASC dimers mediating inflammatory cell death via caspase-1 activation.* Cell Death Differ, 2007. **14**(9): p. 1590-604.

97. Fink, S.L. and B.T. Cookson, *Caspase-1-dependent pore formation during pyroptosis leads to osmotic lysis of infected host macrophages.* Cell Microbiol, 2006. **8**(11): p. 1812-25.

98. Liu, S., et al., *Necroptosis mediates TNF-induced toxicity of hippocampal neurons.* Biomed Res Int, 2014. **2014**: p. 290182.

99. Weber, K., et al., *Nuclear RIPK3 and MLKL contribute to cytosolic necrosome formation and necroptosis.* Commun Biol, 2018. **1**: p. 6.

100. Degterev, A., et al., *Chemical inhibitor of nonapoptotic cell death with therapeutic potential for ischemic brain injury.* Nat Chem Biol, 2005. **1**(2): p. 112-9.

101. Zille, M., et al., *Neuronal Death After Hemorrhagic Stroke In Vitro and In Vivo Shares Features of Ferroptosis and Necroptosis.* Stroke, 2017. **48**(4): p. 1033-1043.

102. Tan, M.S., et al., *Amyloid-beta induces NLRP1-dependent neuronal pyroptosis in models of Alzheimer's disease.* Cell Death Dis, 2014. **5**: p. e1382.

103. Barrington, J., E. Lemarchand, and S.M. Allan, *A brain in flame; do inflammasomes and pyroptosis influence stroke pathology?* Brain Pathol, 2017. **27**(2): p. 205-212.

104. Derry, P.J., et al., *The Chemical Basis of Intracerebral Hemorrhage and Cell Toxicity With Contributions From Eryptosis and Ferroptosis.* Front Cell Neurosci, 2020. **14**: p. 603043.

105. Han, C., et al., *Ferroptosis and Its Potential Role in Human Diseases.* Front Pharmacol, 2020. **11**: p. 239.

106. Li, Q., et al., *Inhibition of neuronal ferroptosis protects hemorrhagic brain.* JCI Insight, 2017. **2**(7): p. e90777.

107. Liang, C., et al., *Recent Progress in Ferroptosis Inducers for Cancer Therapy.* Adv Mater, 2019. **31**(51): p. e1904197.

108. Maher, P., A. Currais, and D. Schubert, *Using the Oxytosis/Ferroptosis Pathway to Understand and Treat Age-Associated Neurodegenerative Diseases.* Cell Chem Biol, 2020. **27**(12): p. 1456-1471.

109. Weiland, A., et al., *Ferroptosis and Its Role in Diverse Brain Diseases.* Mol Neurobiol, 2019. **56**(7): p. 4880-4893.

110. Hirschhorn, T. and B.R. Stockwell, *The development of the concept of ferroptosis.* Free Radic Biol Med, 2019. **133**: p. 130-143.

111. Ratan, R.R., *The Chemical Biology of Ferroptosis in the Central Nervous System.* Cell Chem Biol, 2020. **27**(5): p. 479-498.

112. Stockwell, B.R., et al., *Ferroptosis: A Regulated Cell Death Nexus Linking Metabolism, Redox Biology, and Disease.* Cell, 2017. **171**(2): p. 273-285.

113. Zhou, S.Y., et al., *Mechanism of Ferroptosis and Its Relationships With Other Types of Programmed Cell Death: Insights for Potential Interventions After Intracerebral Hemorrhage.* Front Neurosci, 2020. **14**: p. 589042.

114. Latunde-Dada, G.O., *Ferroptosis: Role of lipid peroxidation, iron and ferritinophagy.* Biochim Biophys Acta Gen Subj, 2017. **1861**(8): p. 1893-1900.

115. McCarus, S.D. and L.K.S. Parnell, *The Origin and Evolution of the HARMONIC(R) Scalpel.* Surg Technol Int, 2019. **35**: p. 201-213.

116. Gruetzmacher, J., *Piezoelektrischer kristall mit ultraschal- lkonvergenz.* Z Phys. , 1935. **96**: p. 342-349.

117. *Radiology key*. Chapter 12: Ultrasound Safety 2016.

118. Wood, R.W.L., A.L., *The physical and biological effects of high-frequency sound waves of great intensity.* Phil. Mag., 1927.

119. Bing, C., et al., *Localised hyperthermia in rodent models using an MRI-compatible high-intensity focused ultrasound system.* Int J Hyperthermia, 2015. **31**(8): p. 813-22.

120. Guillemin, P.C., et al., *Mild hyperthermia by MR-guided focused ultrasound in an ex vivo model of osteolytic bone tumour: optimization of the spatio-temporal control of the delivered temperature.* J Transl Med, 2019. **17**(1): p. 350.

121. Lele, P.P. and K.J. Parker, *Temperature distributions in tissues during local hyperthermia by stationary or steered beams of unfocused or focused ultrasound.* Br J Cancer Suppl, 1982. **5**: p. 108-21.

122. Santos, M.A., et al., *Microbubble-assisted MRI-guided focused ultrasound for hyperthermia at reduced power levels.* Int J Hyperthermia, 2018. **35**(1): p. 599-611.

123. Zhu, L., et al., *Characterization of magnetic resonance-guided high-intensity focused ultrasound (MRgHIFU)-induced large-volume hyperthermia in deep and superficial targets in a porcine model.* Int J Hyperthermia, 2020. **37**(1): p. 1159-1173.

124. Gavrilov, L.R., *Use of focused ultrasound for stimulation of nerve structures.* Ultrasonics, 1984. **22**(3): p. 132-8.

125. Rinaldi, P.C., et al., *Modification by focused ultrasound pulses of electrically evoked responses from an in vitro hippocampal preparation.* Brain Res, 1991. **558**(1): p. 36-42.

126. Min, B.K., et al., *Focused ultrasound-mediated suppression of chemically-induced acute epileptic EEG activity.* BMC Neurosci, 2011. **12**: p. 23.

127. Burgess, A. and K. Hynynen, *Microbubble-Assisted Ultrasound for Drug Delivery in the Brain and Central Nervous System.* Adv Exp Med Biol, 2016. **880**: p. 293-308.

128. Etame, A.B., et al., *Focused ultrasound disruption of the blood-brain barrier: a new frontier for therapeutic delivery in molecular neurooncology.* Neurosurg Focus, 2012. **32**(1): p. E3.

129. McMahon, D. and K. Hynynen, *Acute Inflammatory Response Following Increased Blood-Brain Barrier Permeability Induced by Focused Ultrasound is Dependent on Microbubble Dose.* Theranostics, 2017. **7**(16): p. 3989-4000.

130. Olumolade, O.O., et al., *Longitudinal Motor and Behavioral Assessment of Blood-Brain Barrier Opening with Transcranial Focused Ultrasound.* Ultrasound Med Biol, 2016. **42**(9): p. 2270-82.

131. Phenix, C.P., et al., *High intensity focused ultrasound technology, its scope and applications in therapy and drug delivery.* J Pharm Pharm Sci, 2014. **17**(1): p. 136-53.

132. Yulug, B., L. Hanoglu, and E. Kilic, *The neuroprotective effect of focused ultrasound: New perspectives on an old tool.* Brain Res Bull, 2017. **131**: p. 199-206.

133. Paliwal, S. and S. Mitragotri, *Ultrasound-induced cavitation: applications in drug and gene delivery.* Expert Opin Drug Deliv, 2006. **3**(6): p. 713-26.

134. Miller, M.W., D.L. Miller, and A.A. Brayman, *A review of in vitro bioeffects of inertial ultrasonic cavitation from a mechanistic perspective.* Ultrasound Med Biol, 1996. **22**(9): p. 1131-54.

135. Chu, P.C., et al., *Focused Ultrasound-Induced Blood-Brain Barrier Opening: Association with Mechanical Index and Cavitation Index Analyzed by Dynamic Contrast-Enhanced Magnetic-Resonance Imaging.* Sci Rep, 2016. **6**: p. 33264.

136. Gourevich, D., et al., *In Vitro Investigation of the Individual Contributions of Ultrasound-Induced Stable and Inertial Cavitation in Targeted Drug Delivery.* Ultrasound Med Biol, 2015. **41**(7): p. 1853-64.

137. Chen, H. and E.E. Konofagou, *The size of blood-brain barrier opening induced by focused ultrasound is dictated by the acoustic pressure.* J Cereb Blood Flow Metab, 2014. **34**(7): p. 1197-204.

138. Kovacs, Z.I., S.R. Burks, and J.A. Frank, *Focused ultrasound with microbubbles induces sterile inflammatory response proportional to the blood brain barrier opening: Attention to experimental conditions.* Theranostics, 2018. **8**(8): p. 2245-2248.

139. Sinharay, S., et al., *In vivo imaging of sterile microglial activation in rat brain after disrupting the blood-brain barrier with pulsed focused ultrasound: [18F]DPA-714 PET study.* J Neuroinflammation, 2019. **16**(1): p. 155.

140. Li, J.W., et al., *Microglial priming in Alzheimer's disease.* Ann Transl Med, 2018. **6**(10): p. 176.

141. Perry, V.H. and C. Holmes, *Microglial priming in neurodegenerative disease.* Nat Rev Neurol, 2014. **10**(4): p. 217-24.

142. Lee, T.H., et al., *Improved thrombolytic effect with focused ultrasound and neuroprotective agent against acute carotid artery thrombosis in rat.* Sci Rep, 2017. **7**(1): p. 1638.

143. Burgess, A., et al., *High-intensity focused ultrasound (HIFU) for dissolution of clots in a rabbit model of embolic stroke.* PLoS One, 2012. **7**(8): p. e42311.

144. Papadopoulos, N., C. Yiallouras, and C. Damianou, *The Enhancing Effect of Focused Ultrasound on TNK-Tissue Plasminogen Activator-Induced Thrombolysis Using an In Vitro Circulating Flow Model.* J Stroke Cerebrovasc Dis, 2016. **25**(12): p. 2891-2899.

145. Saletes, I., et al., *In vitro demonstration of focused ultrasound thrombolysis using bifrequency excitation.* Biomed Res Int, 2014. **2014**: p. 518787.

146. Lynn, J.G. and T.J. Putnam, *Histology of Cerebral Lesions Produced by Focused Ultrasound.* Am J Pathol, 1944. **20**(3): p. 637-49.

147. Linke, C.A., et al., *Localized tissue destruction by high-intensity focused ultrasound.* Arch Surg, 1973. **107**(6): p. 887-91.

148. Tarantal, A.F. and D.R. Canfield, *Ultrasound-induced lung hemorrhage in the monkey.* Ultrasound Med Biol, 1994. **20**(1): p. 65-72.

149. Crystal M. D. Collier, M.C., Roger O. Bautista, Robin JI, Hairong Zhang, Elisa E. Konofagou, Carol M. Troy. *Applying High-Intensity Focused Ultrasound to Model Symptomatic and Asymptomatic Intracerebral Hemorrhage in Mice*. in *Cold Spring Harbor Lab Blood Brain Barrier Meeting* 2021. Cold Spring Harbor NY.

150. Crystal M. D. Collier, R.J., Hairong Zhang, Elisa E. Konofagou, Carol M. Troy. *Focused Ultrasound-Induced Intracerebral Hemorrhage at Two Distinct Pressures Causes Differing Outcomes in Mice*. in *Society For Neuroscience*. 2019. Chicago.

151. Elster, A.D., W.T. Sobol, and W.H. Hinson, *Pseudolayering of Gd-DTPA in the urinary bladder.* Radiology, 1990. **174**(2): p. 379-81.

152. Bradley, W.G., Jr., *MR appearance of hemorrhage in the brain.* Radiology, 1993. **189**(1): p. 15-26.

153. Mracsko, E. and R. Veltkamp, *Neuroinflammation after intracerebral hemorrhage.* Front Cell Neurosci, 2014. **8**: p. 388.

154. Ballantine, H.T., Jr., et al., *Focal destruction of nervous tissue by focused ultrasound: biophysical factors influencing its application.* J Exp Med, 1956. **104**(3): p. 337-60.

155. Haelewyn, B., et al., *Long-term evaluation of sensorimotor and mnesic behaviour following striatal NMDA-induced unilateral excitotoxic lesion in the mouse.* Behav Brain Res, 2007. **178**(2): p. 235-43.

156. Stroke Therapy Academic Industry, R., *Recommendations for standards regarding preclinical neuroprotective and restorative drug development.* Stroke, 1999. **30**(12): p. 2752-8.

157. Vyas, M.V., et al., *Stroke Incidence by Sex Across the Lifespan.* Stroke, 2021. **52**(2): p. 447-451.

158. Engler-Chiurazzi, E.B., M. Singh, and J.W. Simpkins, *From the 90's to now: A brief historical perspective on more than two decades of estrogen neuroprotection.* Brain Res, 2016. **1633**: p. 96-100.

159. Selvaraj, U.M., et al., *Selective Nonnuclear Estrogen Receptor Activation Decreases Stroke Severity and Promotes Functional Recovery in Female Mice.* Endocrinology, 2018. **159**(11): p. 3848-3859.

160. Ma, W., Z. Miao, and M.V. Novotny, *Role of the adrenal gland and adrenal-mediated chemosignals in suppression of estrus in the house mouse: the lee-boot effect revisited.* Biol Reprod, 1998. **59**(6): p. 1317-20.

161. Macellari, F., et al., *Neuroimaging in intracerebral hemorrhage.* Stroke, 2014. **45**(3): p. 903-8.

162. Fluri, F., M.K. Schuhmann, and C. Kleinschnitz, *Animal models of ischemic stroke and their application in clinical research.* Drug Des Devel Ther, 2015. **9**: p. 3445-54.

163. Kokiko-Cochran, O.N. and J.P. Godbout, *The Inflammatory Continuum of Traumatic Brain Injury and Alzheimer's Disease.* Front Immunol, 2018. **9**: p. 672.

Apendix 1: FUS-ICH 2.5 in Microglial Caspase 8 KO mice

The FUS-ICH model shows alterations in microglial morphology and CD68 content suggestive of microglial activation. Therapeutics that interfere with microglial activation have shown promise in preclinical models of intracerebral hemorrhage[49, 83]. Caspase-8 has been reported to play a pivotal role in microglial activation through a caspase-3 and -7 dependent pathway[76]. To determine whether caspase-8 is required for microglial activation in response to FUS-ICH as well as to determine the role of microglial caspase-8 in FUS-ICH pathophysiology, we subjected inducible microglia-specific caspase-8 KO mice and caspase-8 floxed littermates lacking the microglial Cre to FUS-ICH at 2.5 MPa. Preliminary results suggest a decrease in the size of the hematoma in mice lacking microglial caspase-8 compared to caspase-8 competent littermates (Fig A1).

Figure A1: FUS-ICH 2.5 with reduced hemorrhage in Microglial Caspase 8 KO mice

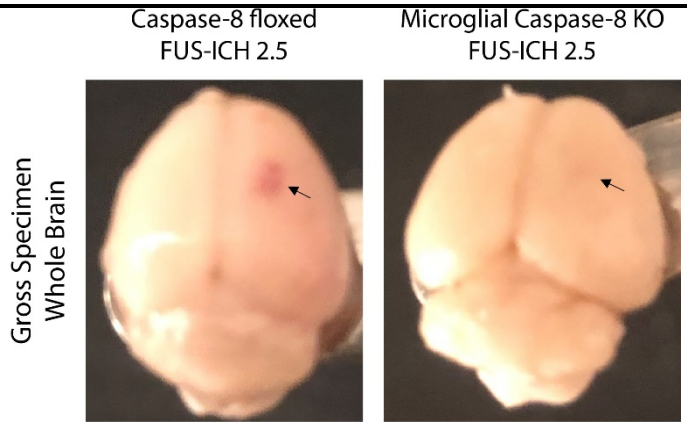

Whole Brain Showing hemorrhage [black arrow] with less appreciable hemorrhage in microglial caspase-8 KO mice (right) compared to caspase-8 floxed littermates (left).

These results pose an intriguing potential for targeting caspase-8 to modulate intracerebral hemorrhage, however substantial additional investigation will be required to determine whether

there is true protection in the microglial caspase-8 condition and to determine the involved mechanism if protection is discovered.